A Systematic Approach to Modeling Impedances and Current Distribution in Planar Magnetics

Minjie Chen, *Student Member, IEEE*, Mohammad Araghchini, *Member, IEEE*, Khurram K. Afridi, *Member, IEEE*, Jeffrey H. Lang, *Fellow, IEEE*, Charles R. Sullivan, *Fellow, IEEE*, and David J. Perreault, *Fellow, IEEE*

***Abstract*—Planar magnetic components using printed circuit board (pcb) windings are attractive due to their high repeatability, good thermal performance, and usefulness for realizing intricate winding patterns. To enable higher system integration at high switching frequency, more sophisticated methods that can rapidly and accurately model planar magnetics are needed. This paper develops a systematic approach to modeling impedances and current distribution in planar magnetics based on a lumped circuit model named as the *modular layer model* (MLM). Stacked pcb layers are modeled as repeating modular impedance networks, with additional modular impedances representing the magnetic core, air gaps, and vias. The model captures skin and proximity effects, and enables accurate predictions of impedances, losses, stored reactive energy, and current sharing among windings. The MLM can be used to simulate circuits incorporating planar magnetics, to visualize the electromagnetic fields, and to extract parameters for magnetic models by simulations, among many other applications. The modeling results are checked with results of previous theories and finite-element-modeling approaches, with good matching presented. A group of planar magnetic devices, including transformers and inductors with various winding patterns, are prototyped, and measured to validate the proposed approach and clarify the boundaries of its applicability.**

***Index Terms*—1-D methods, analytical approach, current distribution, impedances, lumped circuit model, Maxwell's equations, planar magnetics.**

I. Introduction

FOR inductors and transformers in high-frequency power conversion applications, windings fabricated in a printed circuit board (pcb) process with ferrite cores assembled through holes in the board have become a popular strategy. We use the term *planar magnetics* for this approach, which offers high repeatability, good thermal performance, and ease of realizing intricate winding patterns [1]–[4]. These advantages make planar magnetics attractive as switching frequencies increase [5]–[7]. However, the increasing skin and proximity effects and the resulting self and mutual impedances make modeling challenging, especially when parallel windings are included. Previous modeling efforts have estimated ac resistance [8]–[14], predicted parasitics [15]–[17], estimated core losses [18]–[24], extracted parameters by experimental measurements [25], [26], and investigated current sharing among multiple windings [27]–[31]. This has been achieved through means including models using optical system analogies [32]–[36] and discretization-oriented methods [37]–[42], among other approaches. These approaches have different focuses, rely on various assumptions, and sometimes are not easy to use. Numerical methods [e.g., finite-element modeling (FEM)] [43]–[46] and experimental measurements are widely applicable, but are not analytical and are time consuming for design optimization. A systematic approach to modeling planar magnetics, which is fully analytical with low computational requirements, provides intuitive insights, and is capable of capturing many parameters under a minimized assumption setup, is needed and is the main focus of this paper.

Models for planar magnetics commonly share two assumptions, in addition to other case-by-case assumptions. The first common assumption is the "1-D" assumption, under which the electromagnetic field and current distribution within and around the conductor change only along the thickness of the conductor (or insulator). This assumption is satisfied in many designs using high-permeability cores as discussed in detail in Section VI. The second assumption is the "magneto-quasi-static (MQS)" assumption: the electromagnetic field in the planar structure satisfies the MQS requirements [47]–[51], in which the time derivative of the electric field (i.e., capacitive effect) can be decoupled from the other terms in Maxwell's equations and modeled separately with other specific approaches. In a majority of power electronics applications, the MQS assumption is satisfied.

The presented approach requires, and only requires, these two assumptions. The electromagnetic interactions within and among the windings of a planar structure are expressed using the MQS version of Maxwell's equations. These equations are converted into a lumped circuit model with element values explicitly determined by solutions to diffusion equations. The lumped circuit model bridges the circuit domain and the electromagnetic domain; it allows the electromagnetic field and current distributions to be easily calculated, provides insights into the magnetic structure design, and is useful for analyzing circuits incorporating planar magnetic devices. The modeling approach is applicable to a wide variety of devices, from inductors and

Manuscript received October 19, 2014; revised January 14, 2015; accepted February 20, 2015. Date of publication March 11, 2015; date of current version September 21, 2015. This work was supported by the Texas Instruments and the MIT Center for Integrated Circuits and Systems. Recommended for publication by Associate Editor F. Costa.

M. Chen, M. Araghchini, J. H. Lang, and D. J. Perreault are with the Department of Electrical Engineering and Computer Science, Massachusetts Institute of Technology, Cambridge, MA 02139 USA (e-mail: minjie@mit.edu; araghchini@gmail.com; lang@mit.edu; djperrea@mit.edu).

K. K. Afridi is with the Department of Electrical, Computer, and Energy Engineering, University of Colorado Boulder, Boulder, CO 80309 USA (e-mail: khurram.afridi@colorado.edu).

C. R. Sullivan is with the Thayer School of Engineering, Dartmouth College, Hanover, NH 03755 USA (e-mail: charles.r.sullivan@dartmouth.edu).

Color versions of one or more of the figures in this paper are available online at http://ieeexplore.ieee.org.

Digital Object Identifier 10.1109/TPEL.2015.2411618

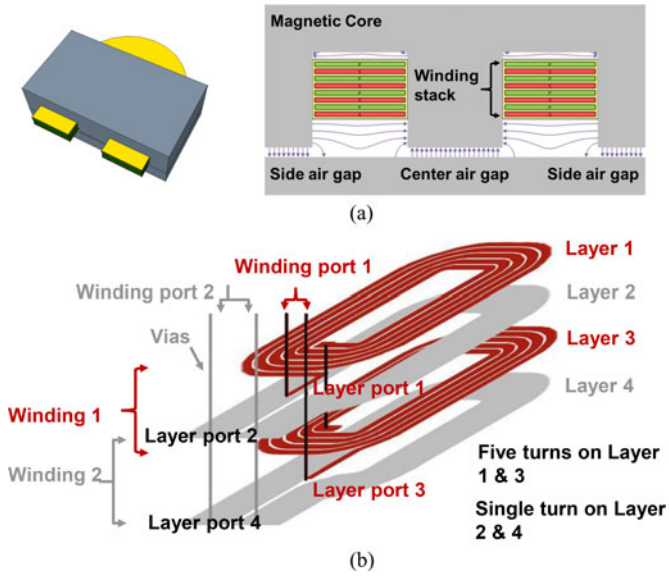

Fig. 1. (a) Cross-sectional view of a planar magnetic structure. It comprises of a magnetic core, a winding stack, and a set of possible air gaps. (b) Example, winding stack of two-winding four-layer transformer with 10:1 turns ratio.

coupled inductors to multiple-winding transformers incorporating interleaving among windings, paralleled windings, and energy storage (e.g., for flyback transformers). The single frequency (fundamental harmonic) behaviors of this lumped circuit model can be rapidly solved by circuit simulators (e.g., SPICE). With some modifications, the lumped circuit is also capable of accurately capturing wideband operation, such as for use in time-domain simulations with many harmonic components. The proposed approach can be applied to various electromagnetic systems, from windings in planar transformers to windings in electric machines.

This paper refines and expands upon our earlier conference publication [52] with updated model derivations, descriptions, and enriched experimental verifications. The paper is organized as follows. Section II outlines the terminology used in this paper, and presents an overview of the proposed approach. A step-by-step derivation of the lumped circuit model is provided in Section III. Section IV explains how the lumped circuit model can be applied to circuit simulations, field visualizations, and parameter/impedance extractions. The proposed approach is verified through FEM simulations and experimental measurements in Section V. Section VI presents the boundaries of applicability of the model, investigates a few practical design constraints, and quantitatively shows the performance of this approach under these constraints. Finally, Section VII summarizes this paper. A detailed derivation of the lumped circuit model is provided in Appendix I, while Appendix II presents theoretical verifications of the proposed approach by comparing it with existing theories.

II. Overview of the Approach

The terminology used in this paper is illustrated in Fig. 1. A planar magnetic structure comprises of a *winding stack*, a *magnetic core*, and a set of possible *air gaps*. A winding stack has one or more *windings*. Each winding comprises of one or more turns on one or more *layers*. Each layer can have multiple *turns*. Usually, turns on the same layer are connected in series. Each layer has a *layer port*. Layer ports are connected by *electrical vias* to form windings. Turns on different layers can be connected in series or parallel, and can be interleaved in various ways. An example of winding stack with two windings and a 10:1 primary-to-secondary turns ratio is shown in Fig. 1(b). It has four layers: layer 1 and layer 3 have five turns each and are connected in series, layer 2 and layer 4 have a single turn each and are connected in parallel.

The proposed approach is developed based on a lumped circuit model—named as the *modular layer model (*MLM)—which utilizes repeating modular impedance networks to represent stacked pcb layers (or other layer stacks). The concept of using modular networks to model magnetic iterations among multiple layers of windings is not new. Here, we highlight two branches of related work to provide the background and clarify the commonalities and differences between the MLM introduced here and other existing circuit models.

Keradec and colleagues modeled multilayer windings in a magnetic component by adapting models for electromagnetic waves propagating in multilayered media, as is sometimes found in optical systems [32]–[36]. Analogies are made between the circuit domain and the optical domain. This model is simple, analytical, and intuitive. However, it requires unwieldy assumptions for the cross-discipline analogies to be fully satisfied. Additional analogies are needed to make the model compatible to other existing models, and/or are applicable to more sophisticated cases. Additional analogies, variable matchings, and unit conversions are required to compare, verify, and extend this approach. Nevertheless, this set of papers introduces a very valuable analytical framework for mapping electromagnetic relationships among layers into connections of three-port circuit blocks, an approach we also adopt.

Lopera *et al.* also developed computational models to capture the behavior of magnetic components comprising electromagnetic fields diffusing through multilayer magnetic windings [37]–[42]. Each layer is discretized into multiple small units. Each unit is represented by a lossy transmission line model. Multiple transmission-line structures are interconnected to model the whole magnetic component. The behavior of the resulting system is found using numerical methods (e.g., with a circuit simulator), essentially placing the burden of solving for the electromagnetic response onto the circuit simulator. This branch of approaches also uses repeating impedance networks to analytically represent layers, but is more similar to FEM because each conductor layer is further discretized. The accuracy of the model depends on the discretization resolution. Empirical design rules are required to choose the appropriate discretization resolution that balances the model complexity and accuracy [41]. The other disadvantage of discretization is that the dependence of the device impedance on the geometry parameters cannot be explicitly expressed using equations. Because the burden of computing the magnetic response (e.g., diffusion of magnetic fields into conductors and the resulting

behavior in the electrical domain) is placed on the circuit simulator, extensive computational resources may be required. An analytical solution would also be especially desirable for situations where large numbers of cases must be run (e.g., as when optimizing winding structures). Nevertheless, discretization enables these group of techniques capturing 2-D cases [39], which is a unique advantage compared to other 1-D analytical methods. Another unique and very useful characteristic of this approach is that its impedance values are not frequency dependent [37].

The proposed approach takes on the advantages of each of the above described models: 1) It is developed directly from basic electromagnetic theories, which allows it to be easily interpreted and rapidly implemented, 2) it relies on very few assumptions; thus, allows us to study the applicability and limitations of this "1-D" and "MQS" analysis framework with minimum constraints, and to further expand the model, 3) it provides analytical solutions for the magnetic fields and resulting electrical characteristics, provides clear design guidelines, and minimizes computational requirements and time, 4) it reexamines many aspects of modeling planar magnetics under a unified set of assumptions, and reveals the underlying connections among many existing approaches. Moreover, we provide clear validated guidelines for where the underlying modeling assumptions hold, including estimates of the degree of error incurred by adopting them, making the approach highly useful in practice. The approach is presented with a focus on emphasizing the physical nature of its analysis framework, while retaining its theoretical integrity, implementation simplicity, modification flexibility, and application generality.

III. Generating the Lumped Circuit Model

The development of the lumped circuit model begins by deriving a modular impedance network for a single turn on a layer (referred to here as a *one-turn layer*). This modular network is repeated and extended to model multiple layers with multiple turns. The magnetic core, the air gaps, and the cross-layer connections (electrical vias) place additional boundary conditions on the impedance networks, and are modeled by additional components in the lumped circuit model. To make the model compatible with circuit analysis, linear conversions (ideal transformers) and electrical interconnects are used to link the electromagnetic domain to the circuit domain.

A. Modeling a One-Turn Layer

Fig. 2(a) shows the geometry of a one-turn layer (e.g., one layer in an E core), with length $\boldsymbol{d}$, width $\boldsymbol{w}$, and thickness $\boldsymbol{h}$. This single turn carries a current $\boldsymbol{I}$ (having current density $\boldsymbol{J}$ with units "$\mathrm{A/m^2}$" pointing toward the *y-axis*, and integrated surface current density, current per width $\boldsymbol{K}$ with units "$\mathrm{A/m}$" distributed along the *x-axis*). This current induces a voltage $\boldsymbol{V}$ across its two terminals. $H_T|H_B$ is the magnetic field ($\boldsymbol{H}$ field) strength on the top|bottom surface of the layer (along the width). $E_T|E_B$ is the electric field ($\boldsymbol{E}$ field) strength on the top|bottom surface of the layer (along the length). As derived in Appendix I-A, solving the 1-D diffusion equation in the conductor under MQS conditions, with the specified boundary conditions [48], and applying *Ohm's Law* ($J{=}\sigma E$, where σ is the conductivity of this conductor) gives the relationship between the magnetic fields and electric fields on the top and bottom surfaces, and the integrated surface current density K carried by this layer

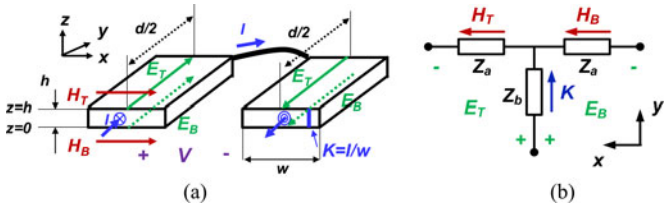

Fig. 2. (a) One-turn layer and (b) its three-terminal impedance network. The positive directions of all variables (H, E, I, V, K, etc.) used in this paper are referred to the x-, y-, z-axes shown in this figure. A positive $E|H$ field in the physical structure is represented by a positive $E|H$ value in the impedance network. The two conductors form a single turn and are connected by a interconnect wire whose impedance is neglected. This one-turn layer is modeled as a three-terminal impedance network.

$$\begin{aligned} E_T &= Z_a H_T + Z_b K \\ \underbrace{E_B}_{\mathrm{V/m}} &= \underbrace{Z_b}_{\Omega}\underbrace{K}_{\mathrm{A/m}} - \underbrace{Z_a}_{\Omega}\underbrace{H_B}_{A/m}. \end{aligned} \tag{1}$$

Here, Z_a and Z_b are two complex impedances (with units of Ω) explicitly determined by the geometry of the structure and the operating angular frequency (ω), and are given by

$$\begin{aligned} Z_a &= \frac{\Psi(1-e^{-\Psi h})}{\sigma(1+e^{-\Psi h})} \\ Z_b &= \frac{2\Psi e^{-\Psi h}}{\sigma(1-e^{-2\Psi h})}. \end{aligned} \tag{2}$$

Here, $\Psi = \frac{1+j}{\delta}$, where $\delta = \sqrt{\frac{2}{\omega\mu\sigma}}$ is the skin depth of the conductor, and μ is its permeability. Also, H_T, H_B, I, and K are related through *Ampere's law*

$$(H_T - H_B)w = I = Kw. \tag{3}$$

All variables (E, H, V, I, Z, etc.) are complex variables. Since H_T, H_B, and K are related to current (units: $\mathrm{A/m}$), E_T and E_B are related to voltage (unit: $\mathrm{V/m}$), and Z_a and Z_b are the impedances (unit: Ω), (1) and (3) can be considered as the *Kirchhoff's voltage law* (KVL) and *Kirchhoff's current law* (KCL) determining a three-terminal impedance network, as shown in Fig. 2(b), with impedance values calculated with (2). A related circuit configuration can be found in [32]. Compared to Keradec's derivation, our derivation is self-consistent without making cross-discipline analogies. Variables and relationships have circuit domain definitions, representing different field-to-circuit mapping relationships. For example, the E field in our derivation is the actual physical electric field commonly used in magnetic modeling (i.e., $E = V/d$). While in Keradec's derivation, optical wave propagation concepts such as "electrostatic field" and "induced electric field" were borrowed.

B. Modeling Two Adjacent Layers

Fig. 3(a) shows the geometry of two adjacent one-turn layers separated by a spacing (created with an insulator) between them.

Based on the previous derivation, the electromagnetic fields around and within each layer can be described by the following two sets of equations:

$$\text{Layer 1:}\quad \begin{cases} E_{T1} = Z_{a1}H_{T1} + Z_{b1}K_1 \\ E_{B1} = Z_{b1}K_1 - Z_{a1}H_{B1} \\ H_{T1} - H_{B1} = K_1 \\ wK_1 = I_1. \end{cases} \qquad \text{Layer 2:}\quad \begin{cases} E_{T2} = Z_{a2}H_{T2} + Z_{b2}K_2 \\ E_{B2} = Z_{b2}K_2 - Z_{a2}H_{B2} \\ H_{T2} - H_{B2} = K_2 \\ wK_2 = I_2. \end{cases} \tag{4}$$

Here, $H_{Ti}|H_{Bi}$ is the magnetic field strength on the top|bottom surface of the layer i; $E_{Ti}|E_{Bi}$ is the electric field strength on the top|bottom surface of layer i; Z_{ai} and Z_{bi} are complex impedances of layer i defined by the geometry and frequency; I_i is the current that is carried by layer i. Based on (4), layer 1 and layer 2 can be represented by two modular impedance networks labeled as "Layer 1" and "Layer 2" in Fig. 3(b). Also labeled are the associated electromagnetic field variables on the top and bottom surfaces of each layer.

The electromagnetic fields surrounding the two layers are related by the magnetic flux flowing in the spacing between them (Φ_{S12}). The spacing has a thickness a_1, width w, and length $\boldsymbol{d}$. From flux continuity, the magnetic field strength in the spacing H_{S12} equals H_{B1} and H_{T2}. Considering the voltage loops on the bottom surface of layer 1, and on the top surface of layer 2 (including layer surfaces, external wires, and sources surrounding the center post), and using *Faraday's Law* and flux continuity (as shown in Appendix I-B), the magnetic flux flowing through the center post across the two surfaces Φ_{B1} and Φ_{T2} can be written as functions of the electric fields on the two layer surfaces (E_{B1}, E_{T2}), as well as the external voltages applied to the two layer ports (V_1 and V_2), such that

$$\begin{cases} j\omega\Phi_{B1} = V_1 - dE_{B1} \\ j\omega\Phi_{T2} = V_2 - dE_{T2} \\ \Phi_{B1} + \Phi_{S12} = \Phi_{T2} \\ H_{S12} = \dfrac{\Phi_{S12}}{\mu_0 a_1 d}. \end{cases} \tag{5}$$

Here, the permeability of the space (insulator) between the two layers is assumed to be μ_0. Thus, the magnetic field in the spacing H_{S12} can be expressed as

$$H_{S12} = \frac{1}{j\omega\mu_0 a_1}\left(\frac{V_2}{d} - E_{T2} - \frac{V_1}{d} + E_{B1}\right). \tag{6}$$

Defining $Z_{S1} = j\omega\mu_0 a_1$ gives

$$\underbrace{H_{S12}}_{\text{A/m}}\underbrace{Z_{S1}}_{\Omega} = \underbrace{\frac{V_2}{d} - E_{T2} - \frac{V_1}{d} + E_{B1}}_{\text{V/m}}. \tag{7}$$

Equation (7) is an important KVL relation that links the two impedance networks. The resulting lumped circuit model for two adjacent layers is shown in Fig. 3(b). Note that the integrated surface current densities K_1 and K_2 need to be linearly converted into external layer currents $I_1 = wK_1$ and $I_2 = wK_2$. These linear conversions are modeled with current-dependent current sources (CDCS) with gains of w (layer width). According to (7), linear conversions are also required to convert the induced layer port voltages V_1 and V_2 to electric fields $\frac{V_1}{d}$ and $\frac{V_2}{d}$. These linear conversions are modeled with voltage-dependent voltage sources (VDVS) with gains of $\frac{1}{d}$. These VDVS and CDCS are paired up for each layer and labeled as "layer ports" in Fig. 3(b).

The modeling of the layer port becomes simpler and more straightforward if we consider a general case when there are multiple series-connected (concentric) turns on one or many layers. Fig. 4(a) shows an example setup with layer 1 having two series-connected turns, and layer 2 having a single turn. In a general case, assume layer i has m_i turns, and all turns have the same width $\frac{w}{m_i}$, thickness h_i, and length d. H_{Ti}, H_{Bi}, and K_i are linearly related to I_i: $I_i = \frac{wK_i}{m_i} = \frac{w(H_{Ti}-H_{Bi})}{m_i}$. Also, the Φ_i on the top|bottom surfaces of layer i is linearly related to E_i and V_i on the top|bottom surfaces $j\omega\Phi_i = \frac{V_i}{m_i} - dE_i$. Equations (4) and (7), which were developed for single-turn layers and were represented with the circuit of Fig. 3(b), generalize to the following set of equations including m_1 and m_2 as parameters:

$$\text{Layer 1}: \begin{cases} \underbrace{dE_{T1}}_{\text{V}} = \underbrace{wH_{T1}}_{\text{A}}\underbrace{\frac{d}{w}Z_{a1}}_{\Omega} + \underbrace{wK_1}_{\text{A}}\underbrace{\frac{d}{w}Z_{b1}}_{\Omega} \\ dE_{B1} = wK_1\frac{d}{w}Z_{b1} - wH_{B1}\frac{d}{w}Z_{a1} \\ H_{T1} - H_{B1} = K_1 \\ wK_1 = I_1 m_1 \end{cases}$$

$$\text{Layer 2}: \begin{cases} dE_{T2} = wH_{T2}\frac{d}{Z_{a2}} + wK_2\frac{d}{w}Z_{b2} \\ dE_{B2} = wK_2\frac{d}{w}Z_{b2} - wH_{B2}\frac{d}{w}Z_{a2} \\ H_{T2} - H_{B2} = K_2 \\ wK_2 = I_2 m_2 \end{cases}$$

$$\text{Spacing}: \underbrace{\frac{V_2}{m_2} - dE_{T2} - \frac{V_1}{m_1} + dE_{B1}}_{\text{V}} = \underbrace{wH_{S12}}_{\text{A}}\underbrace{\frac{d}{w}Z_{S1}}_{\Omega}. \tag{8}$$

These reorganized equations have individual terms having circuit domain units ("V," "A," "Ω"). It can be represented by a clarified lumped circuit model as shown in Fig. 4(b). By linearly scaling all impedances with a geometry factor $\frac{d}{w}$, all dependent sources (VDVS and CDCS) can be replaced by ideal transformers[1] with turns ratios of m_1 and m_2, directly representing the numbers of physical turns on each layer. With these linear conversions,[2] all variables in Fig. 4(b) are entirely in the circuit domain.

[1] This "ideal-transformer" configuration is also utilized in [32] and [37]. However, we rigorously derived it using Maxwell's equations (to provide a proof and to avoid using vague analogy/assumptions), and took this opportunity to convert all variables back to the circuit domain. Presenting all variables in the circuit domain allows the magnetic device integrally analyzed and interpreted with external circuits under a unified system setup (e.g., the current distribution can be directly measured in SPICE simulations). Linear conversions after simulations/computations are avoided. This modeling approach also results in a physical rational ideal-transformer turns ratio that intuitively represents the number of physical turns.

[2] A more intuitive way to interpret these linear relationships is to consider the m_i turns as a single turn having equivalent total width, with its current multiplied by m_i, and its voltage divided by m_i. An ideal transformer with turns ratio of m_i:1 naturally reflects these linear relationships. This interpretation is an additional analogy, but it does not require additional assumption because small

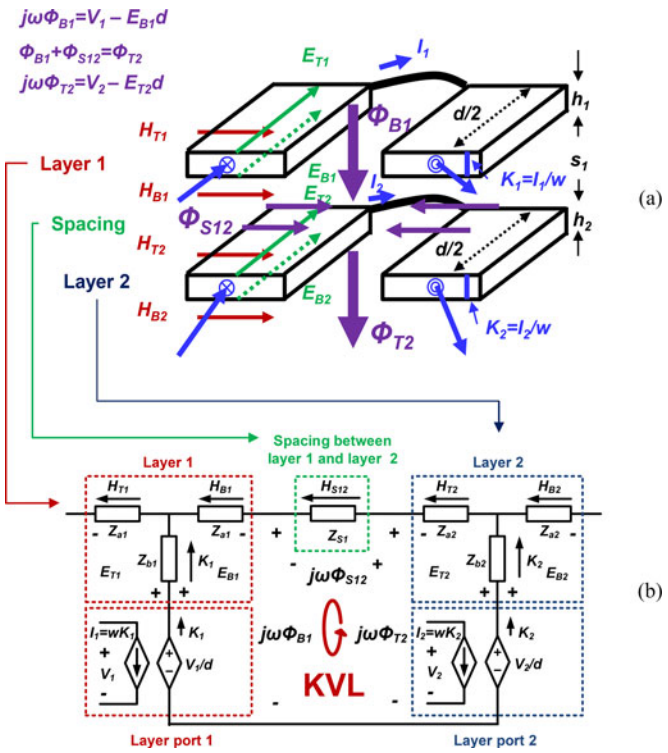

Fig. 3. Two one-turn adjacent layers. (a) Planar geometry and (b) impedance network model with "V/m," "A/m," and "Ω" as the internal units. The variables on one side of the dependent sources are H, E, and K. They are in the electromagnetic domain. The variables on the other side of the dependent sources are voltages and currents. They are in the circuit domain.

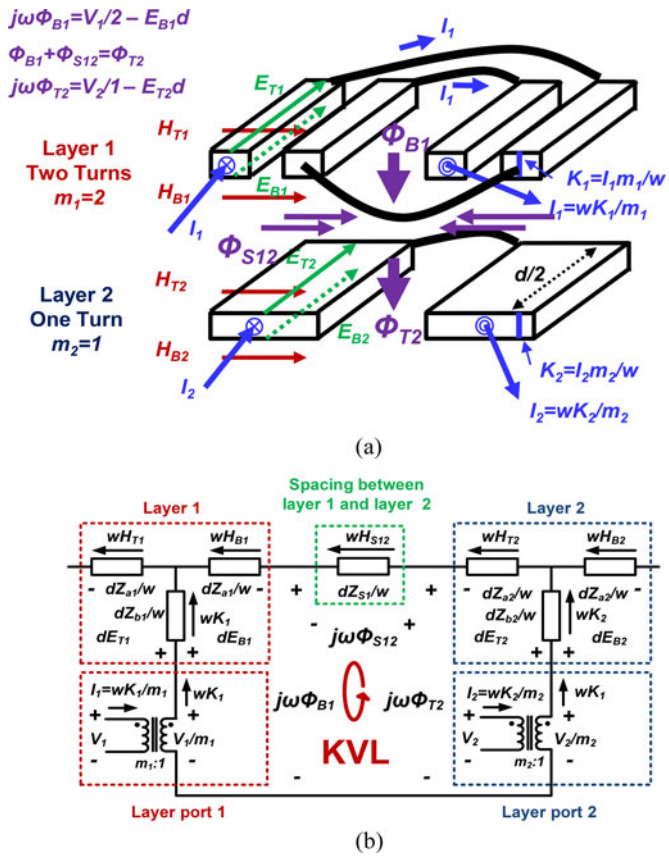

Fig. 4. Two adjacent layers—layer 1 has two series-connected turns ($m_1 = 2$), and layer 2 has a single turn ($m_2 = 1$). (a) Planar geometry and (b) impedance network model with "V," "A," and "Ω" as the internal units. This system is entirely in the circuit domain. The circuit architecture is determined by using Maxwell's equations as KVL and KCL rules. The complex impedances are determined by solutions to 1-D diffusion equation under MQS conditions.

C. Modeling the Magnetic Core and the Air Gaps

Consider a planar structure with n layers, one magnetic core, and two air gaps as shown in Fig. 5. The number of series-connected turns on layer 1 to layer n are m_1 to m_n, respectively. The core has a gap of length g_1 in the outer legs, and a gap of length g_2 in the center post (the total gap length is $g_1 + g_2$). The cross-sectional area of the air gap in the center post is A_c and in the outer surface is $\frac{A_c}{2}$. The thicknesses of layers 1 to n are h_1 to h_n, respectively. The spacing thickness between layer i and layer $(i + 1)$ is a_i. The spacing thickness between the top surface of layer 1 and the magnetic core is b_t. The spacing thickness between the bottom surface of layer n and the magnetic core is b_b. The thickness of the top side of the core is c_t, and the thickness of the bottom side of the core is c_b. The magnetic field strength on the top|bottom surface of the layer i is $H_{Ti}|H_{Bi}$. The electric field strength on the top|bottom surface of layer i is $E_{Ti}|E_{Bi}$. The magnetic flux flowing through the center post across the top|bottom surfaces of layer i is Φ_{Ti} and Φ_{Bi}. The currents that flow through layers 1 to n are I_1 to I_n. The induced voltages of layers 1 to n are V_1 to V_n. The reluctance of the top side of the core is $\mathcal{R}_T$, carrying magnetic flux Φ_T. The reluctance of the bottom side of the core and the air gap is $\mathcal{R}_B$, carrying magnetic flux Φ_B. Note that $\mathcal{R}_T$ and $\mathcal{R}_B$ include the reluctances of the spacings (between the winding stack and the core) and the magnetic core itself. As shown in Fig. 5, Φ_{T1} and Φ_{B1} are the summations of the flux carried by the spacings and the magnetic core ($\Phi_{T1} = \Phi_{ts} + \Phi_T$, $\Phi_{Bn} = \Phi_B - \Phi_{bs}$).

We investigate how to rigorously represent these variables and their relationships in the lumped circuit model. The lumped model for the n conductor layers and the $n-1$ spacings among them can be generated by simply repeating the modular network of each layer and spacings between two conductor layers [simply extending Fig. 4(b)]. The magnetic core and the air gaps impose additional boundary conditions and, hence, add additional circuit elements. Derived from the magnetic reluctance circuit model as shown in Appendix I-C, variables on the top and bottom of the layer stack (E, V, and H) are related by the reluctances of the top and bottom side of the core ($\mathcal{R}_T$ and $\mathcal{R}_B$)

$$\begin{aligned} dE_{T1} - \frac{V_1}{m_1} &= -\frac{j\omega}{\mathcal{R}_T} w H_{T1} \\ dE_{Bn} - \frac{V_n}{m_n} &= \frac{j\omega}{\mathcal{R}_B} w H_{Bn}. \end{aligned} \tag{9}$$

spacings between adjacent turns are implicitly assumed when utilizing the "1-D" assumption. The presented derivation of (8) is a strict theoretical proof for this analogy. As will be experimentally investigated in Section VI, small spacings between adjacent turns on the same layer are required. The relative size of these spacings are usually constrained by pcb manufacturing capability and insulation requirements.

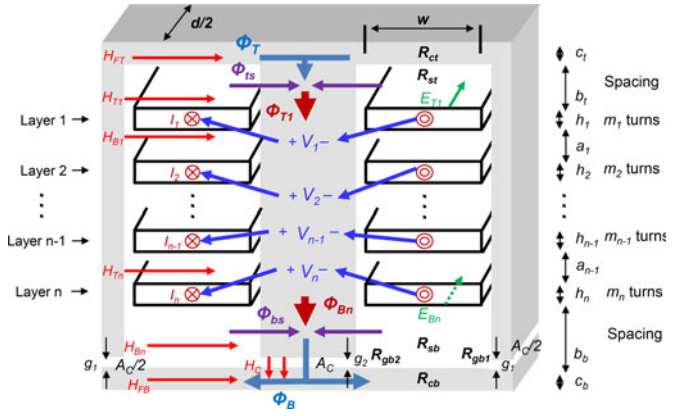

Fig. 5. Planar structure with n layers, a magnetic core, and multiple air gaps, with $g_1 + g_2$ as the total gap length. All layers are drawn as one-turn layers for simplicity. In a general case, layer 1 to layer n have m_1 to m_n series-connected turns. All layers usually have the same length d (determined by the core length) and width w (determined by the window width).

We define two impedances

$$\begin{aligned} Z_T &= j\omega/\mathcal{R}_T \\ Z_B &= j\omega/\mathcal{R}_B. \end{aligned} \tag{10}$$

Equation (9) can be rewritten as

$$\begin{aligned} dE_{T1} - \frac{V_1}{m_1} &= -wH_{T1}Z_T \\ dE_{Bn} - \frac{V_n}{m_n} &= wH_{Bn}Z_B. \end{aligned} \tag{11}$$

As KVL rules, (11) places Z_T and Z_B on the left and right side of the lumped circuit model as shown in Fig. 6. $\mathcal{R}_T$ and $\mathcal{R}_B$ can be calculated as the series/parallel combination of any gap reluctances $\mathcal{R}_{gt}$ and $\mathcal{R}_{gb}$, the core reluctances $\mathcal{R}_{ct}$ and $\mathcal{R}_{cb}$, and the shunt reluctances of the spacings between the winding and the core $\mathcal{R}_{st}$ and $\mathcal{R}_{sb}$

$$\begin{aligned} \mathcal{R}_T &= (\mathcal{R}_{ct} + \mathcal{R}_{gt})||\mathcal{R}_{st} \\ \mathcal{R}_B &= (\underbrace{\mathcal{R}_{cb}}_{\text{core}} + \underbrace{\mathcal{R}_{gb}}_{\text{gap}})|| \underbrace{\mathcal{R}_{sb}}_{\text{spacing}}. \end{aligned} \tag{12}$$

Note that reluctances of the vertical core legs are neglected, based on the assumption of a high-permeability core and/or short lengths of these legs in a planar core shape. For ungapped structures, gap reluctances $\mathcal{R}_{gt}$ and $\mathcal{R}_{gb}$ are zero, leaving only core reluctances. The reluctance of a short gap, that is, a gap with of length g much smaller than the lateral dimensions of the gap, can be approximated by $\mathcal{R}_g \approx \frac{g}{\mu_0 A_c}$. For longer gaps and arbitrary gap distribution, 2-D or 3-D reluctance calculations considering fringing effects, such as those in [53]–[57] should be used. If there are multiple gaps at the top or bottom, $\mathcal{R}_{gt}$ and $\mathcal{R}_{gb}$ are the sums of the reluctances at top and bottom, respectively. For example, in Fig. 5, there is no core gap on the top side, so $\mathcal{R}_{gt}$ equals zero. $\mathcal{R}_{gb}$ is the sum of the reluctances of the two gaps at the bottom center and bottom sides ($\mathcal{R}_{gb}$=$\mathcal{R}_{gb2}$+$\mathcal{R}_{gb1}$/2).

Note the underlying connections between the MLM (focus on the windings), and conventional magnetic reluctance circuit models (focus on cores). As derived in Appendix I-C, if we ignore Z_as, Z_bs, and Z_Ss, and only consider Z_T and Z_B and the layer ports, the lumped circuit model shown in Fig. 6 is equivalent to a topological dual of a conventional magnetic reluctance circuit model [49]–[51]. The inclusion of Z_as, Z_bs, and Z_Ss automatically capture the self-impedance, the mutual impedance, and the skin and proximity effects. The modeling of the winding and the core are rigorously integrated in a unified setup.

The KVL and KCL rules of the circuit shown in Fig. 6 are interchangeable with the electromagnetic constraints imposed by the MQS version of Maxwell's equations. Solving this circuit model is equivalent to solving the Maxwell's equations. All impedances are calculated explicitly with formulas using the geometry of the planar structure and the operating frequency. All parameters (m_i, d, w, h_i, etc.) have clear physical meanings. All physical variables (V_i, I_i, wH_{Bi}, wH_{Ti}, Φ_{Ti}, Φ_{Bi}, etc.) are mapped one-to-one with across and through variables (voltages and currents) in the circuit model and can be found by circuit analysis. All units are compatible with electrical circuit analysis methods (measured in "V," "A," and "Ω"). Since the model is rigorously derived based on the 1-D and MQS assumption without using additional analogies/assumptions, the modeling of each element of the system are strictly compatible with other existing techniques specified for each individual element. For example, resistances in shunt with Z_Ts and Z_Bs, calculated using conventional core loss estimation approach, can be included to capture the core loss and its impacts on winding loss. The nonlinear characteristics of the core can be modeled by replacing Z_T and Z_B with nonlinear impedances.

D. Modeling Cross-Layer Connections

In a pcb magnetics with many turns, multiple layers are usually connected by cross-layer connections (electrical vias) in series or parallel to form complete windings. Layers of different windings can be interleaved in multiple ways. These electrical vias brings additional constraints, and can be realized by connecting the corresponding layer ports in the same pattern as they are connected in the physical circuit. For example, consider the case where layer i and layer j are connected in series to form winding a, driven by voltage V_a and carrying current I_a, and layer k and layer l are connected in parallel to form winding b, driven by voltage V_b and carrying net current I_b. The following four KCL or KVL constraints:

$$\begin{cases} V_i + V_j = V_a \\ V_k = V_l = V_b \\ I_i = I_j = I_a \\ I_k + I_l = I_b \end{cases} \tag{13}$$

are added to the existing Maxwell's equations [i.e., (8) and (11). These constraints can be naturally included in the lumped circuit model by connecting the layer ports of layer i and layer j in series, and connecting the layer ports of layer k and layer l in parallel, as shown in Fig. 7.

Note that this treatment does not include the impedances of the cross-layer interconnects and interwinding capacitances.

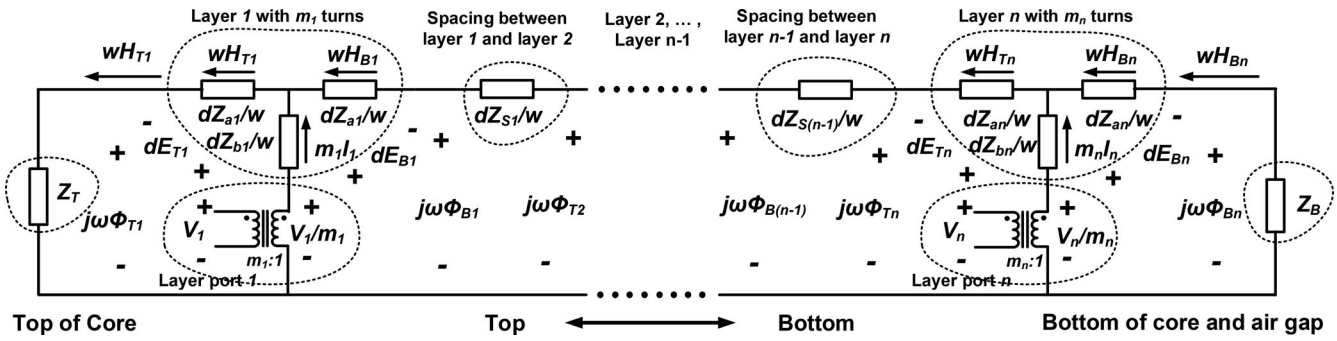

Fig. 6. Lumped circuit model for a planar magnetic structure with n windings, a magnetic core, and multiple air gaps as shown in Fig. 5. The n layers from top to bottom in the physical geometry are mapped one-to-one to the n modular impedance networks from left to right in the lumped circuit model. The additional constraints brought by the top and bottom magnetic core and air gaps place additional impedances (Z_T and Z_B) on the left and right sides of the n modular impedance networks.

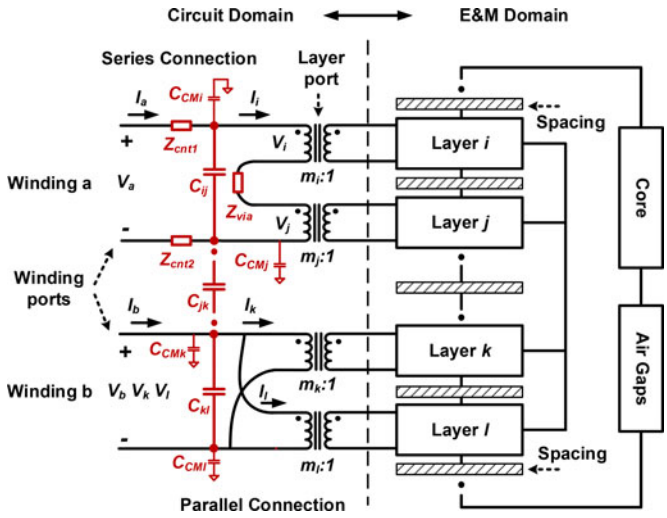

Fig. 7. Model showing cross-layer connections (electrical vias) of the layer ports to formulate windings. Layers i and j are connected in series, and layers k and l are connected in parallel. Modular impedance networks are drawn as blocks. A few example places holders for modeling the impedances of the interconnects (z_{ts1}, z_{ts2}), vias ($z_{\rm via}$), and parasitic capacitances (common mode, differential mode) are also shown. The interconnect impedances and parasitic capacitance values can be estimated using techniques such as those developed in [58] and [59].

Without making additional assumptions/approximations (that may violate the "1-D" or "MQS" assumption), these effects cannot be rigorously included under this analysis framework and, thus, are beyond the capability of this lumped circuit model. In many designs, the cross-layer interconnects and capacitances can be approximated by isolating the electro-quasi-static (EQS) and MQS characteristics [48] and, thus, be modeled as additional impedances that are not mutually correlated with those already modeled impedances. A few example place holders for impedances of the interconnects ($Z_{\rm cnt1}$, $Z_{\rm cnt2}$), vias ($Z_{\rm via}$), and cross-layer capacitances (C_{ij}, C_{jk}, etc.) are shown in Fig. 7. Classic impedance calculation methods in radio-frequency engineering [58] and power electronics [59] can be utilized to find approximate values of these impedances. This treatment is generally applicable in power electronics applications, while specific accuracy/limitations require case-by-case evaluation.

E. Summary of the Lumped Circuit Model

The generation of the lumped circuit model can be summarized as a step-by-step procedure. All variables are the same as previously defined.

1) Conductor Layers: Each conductor layer i is modeled as a three-terminal impedance network comprising two "horizontal" impedances $\frac{d}{w}Z_{ai}$ and one "vertical" impedance $\frac{d}{w}Z_{bi}$. The values of Z_{ai} and Z_{bi} are determined by the thickness (h_i) of this layer, parameters of the conductive material (μ_i, σ_i), the angular operating frequency (ω), $\Psi_i = \frac{1+j}{\delta_i}$, and $\delta_i = \sqrt{\frac{2}{\omega\mu_i\sigma_i}}$, according to

$$Z_{ai} = \frac{\Psi_i(1-e^{-\Psi_i h_i})}{\sigma_i(1+e^{-\Psi_i h_i})}$$
$$Z_{bi} = \frac{2\Psi_i e^{-\Psi_i h_i}}{\sigma_i(1-e^{-2\Psi_i h_i})}. \tag{14}$$

The geometry factor of $\frac{d}{w}$ is applied to Z_{ai} and Z_{bi} to bring the results into the circuit domain. Under the 1-D assumption, all layers can be approximated to have the same effective length d and total width w, although they may have different numbers of series-connected turns (m_i). The clearances between two adjacent turns on the same layer and between the conductor and the ferrite core should be minimized. The impacts of these clearances are investigated in Section VI-B.

2) Layer Ports: Each conductor layer has a layer port. It performs linear conversions, and allows connections to other layers through electrical vias. The interconnection into the electromagnetic model at the layer port is realized with an ideal transformer, whose turns ratio equals the number of series-connected turns on that layer (m_i:1).

3) Spacings: The spacings between adjacent layers are modeled by impedances. The interconnect impedance between layer i and layer $(i+1)$ is $\frac{d}{w}Z_{Si}$, where

$$Z_{Si} = j\omega\mu_i a_i. \tag{15}$$

Here, the spacing between layer i and layer $(i+1)$ has thickness of a_i and permeability of μ_i.

4) Magnetic Core and Air Gaps: The effect of the magnetic core and air gaps is modeled by additional impedances on both

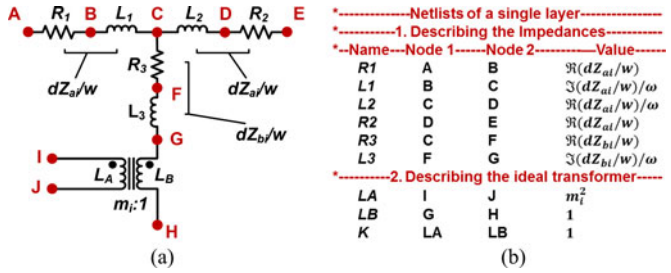

Fig. 8. Modular impedance network and its netlist for a layer with m_i turns. Here, $\Re$ represents the real part of a complex value, and $\Im$ represents the imaginary part of a complex value.

sides of the circuit. The impedances representing the top and bottom of the magnetic core are Z_T and Z_B, where

$$Z_T = j\omega/\mathcal{R}_T \qquad Z_B = j\omega/\mathcal{R}_B. \tag{16}$$

Here, $\mathcal{R}_T$ and $\mathcal{R}_B$ are the reluctances of the top and bottom of the core, respectively, including the reluctance of any gaps in the core in each of those positions. Core loss and its impacts can be captured by adding appropriate shunt resistances.

5) Cross-Layer Connections: The final step is to connect the layer ports of all modular impedance network in the same pattern as they are connected in the physical circuits. Cross-layer capacitances and interconnect impedances can be modeled as independent elements as shown in Fig. 7.

The lumped circuit model is completed up to this step. This model has frequency-dependent impedances, and thus can only rigorously capture single-frequency behaviors. The model can be applied in fundamental harmonic analysis even when significant harmonics are presented. The modeling accuracy is usually sufficient for making preliminary engineering design choices. Further expansions can be made to model systems with wide-frequency range by various known techniques. One way is to simply repeat the modeling approach at each independent frequency of interest (utilized in this paper). The other way is to generate more complicated impedance networks to capture behavior over a wide-frequency range. Methods in this type include simple first- or second-order approximate networks [32], and discretized numerically fitted networks [38]. Designers can make tradeoffs between model simplicity and accuracy by choosing and mixing these techniques.

IV. Applications

A. Generating Netlists for Circuit Simulation

The lumped circuit model shown in Fig. 6 (and shown in Fig. 7 with cross-layer connections included) can be solved analytically. More conveniently, it can be described by a netlist, and directly solved with a circuit simulator, such as SPICE. For example, a layer with m_i series-connected turns can be represented by a lumped circuit model as shown in Fig. 8(a), and described by a netlist as shown in Fig. 8(b). Since the generation of the lumped circuit model follows a step-by-step procedure, the full netlist of the pcb magnetics can be rapidly synthesized by a computer program,[3] which calculates the impedance values based on geometry information and exports a netlist. Circuit simulations can be used to determine the current flowing through each winding and each layer, to calculate the magnetic field strengths at the surface of each conductor, to predict the loss on each layer, and to perform small signal analysis between two ports. Since the impedance values are calculated analytically and explicitly using the solutions to 1-D diffusion equations, this circuit simulation captures the skin and proximity effects, allowing impedances, losses, reactive energy, current sharing, etc., to be determined with the magnetics netlists simulated with the circuits.

B. Field Visualization

This lumped circuit model also provides insight into the design of the magnetic structure. Fields at the surfaces of conductors solved using the lumped circuit model (i.e., H_T, H_B, and K) can be used in calculating the fields and current densities inside the conductors using known formulations. For example, based on knowing the fields at the conductor surfaces (H_T and H_B) and the solutions to 1-D diffusion equations (Appendix I-A), the H field strength inside the conductor as a function of the distance from the surfaces can be found by

$$H_x(z) = \frac{H_T \sinh(\Psi z) + H_B \sinh(\Psi(h-z))}{\sinh(\Psi h)}. \tag{17}$$

Note $H_x(z)$ points toward the *x-axis*, and varies along the *z-axis* (the axes directions were defined in Fig. 2). Using *Ampere's law* $J_y(z) = \nabla \times H_x(z)$, the current density distribution in the conductor $J_y(z)$ is

$$J_y(z) = \Psi\left[\frac{H_T e^{\Psi h} - H_B}{e^{\Psi h} - e^{-\Psi h}} e^{-\Psi(h-z)} - \frac{H_B e^{\Psi h} - H_T}{e^{\Psi h} - e^{-\Psi h}} e^{-\Psi z}\right]. \tag{18}$$

The loss in each layer can be calculated by $\frac{wd}{2\sigma}\int_0^h |J_y(z)|^2 dz$. Finally, using *Ohm's Law* $J_y = \sigma E_y$, the electric field distribution inside the conductor $E_y(z)$ is

$$E_y(z) = \frac{\Psi}{\sigma}\left[\frac{H_T e^{\Psi h} - H_B}{e^{\Psi h} - e^{-\Psi h}} e^{-\Psi(h-z)} - \frac{H_B e^{\Psi h} - H_T}{e^{\Psi h} - e^{-\Psi h}} e^{-\Psi z}\right]. \tag{19}$$

Hence, the field distribution and the current densities in the magnetic structure, within and outside the conductors along the thickness (z) direction, can be rapidly and explicitly solved and visualized (as demonstrated in Fig. 22).

C. Parameter/Impedance Extraction by Simulation

Numerous ways of modeling magnetic devices with simpler circuit models have been developed [47]–[51]. To determine the parameters of many of these models, experimental measurements are required. For example, open- and short-circuit measurements are used to extract the parameters of the inductance

[3] A software that can generate SPICE netlists based on geometry information is accessible by emailing the authors (or search for keyword "M2Spice").

TABLE I
CALCULATED LOSS IN THE FOUR LAYERS OF THE "ALTERNATING" AND "SYMMETRIC" INTERLEAVED TRANSFORMERS UNDER THE SETUP OF FIG. 11(B), WHEN THEY ARE OPERATING AT 10 AND 100 MHZ, AND DRIVEN BY A 1-A RMS SINUSOIDAL CURRENT IN THE TWO SERIES-CONNECTED LAYERS AND A REVERSE 2-A RMS SINUSOIDAL CURRENT IN THE TWO PARALLEL-CONNECTED LAYERS

Loss in Each Layer # (mW)	#1	#2	#3	#4	Total
Alternating, 10 MHz	24.7	79.6	24.1	0.7	129.1
Symmetric, 10 MHz	24.7	24.7	24.7	24.7	98.8
Alternating, 100 MHz	62.7	100.3	44.4	1.7	209.1
Symmetric, 100 MHz	62.7	62.7	62.7	62.7	250.8

White: series-connected layers; Grey: parallel-connected layers.

TABLE II
EXTRACTED IMPEDANCE MATRICES OF THE "ALTERNATING" AND "SYMMETRIC" INTERLEAVED TRANSFORMERS, WHEN THEY ARE OPERATING AT 10 AND 100 MHZ

$\mathbf{Z}$, unit : Ω	defined as: $\begin{pmatrix} V_a \\ V_b \end{pmatrix} = \mathbf{Z} \times \begin{pmatrix} I_a \\ I_b \end{pmatrix}$
Alternating, 10 MHz	$\begin{pmatrix} 24.253 + 28\,417j & 12.052 + 14\,208j \\ 12.052 + 14\,208j & 6.0487 + 7\,104.9j \end{pmatrix}$
Symmetric, 10 MHz	$\begin{pmatrix} 24.153 + 28\,416j & 12.036 + 14\,208j \\ 12.036 + 14\,208j & 6.0408 + 7\,105.6j \end{pmatrix}$
Alternating, 100 MHz	$\begin{pmatrix} 2\,406.3 + 284\,150j & 1\,203.1 + 142\,070j \\ 1\,203.1 + 142\,070j & 601.63 + 71\,043j \end{pmatrix}$
Symmetric, 100 MHz	$\begin{pmatrix} 2\,406.3 + 284\,144j & 1\,203.1 + 142\,071j \\ 1\,203.1 + 142\,071j & 601.70 + 71\,051j \end{pmatrix}$

matrix [49] and inductance-based cantilever model [26]. Well conducted experimental measurements undoubtedly capture the most information. However, the accuracy of experimental measurements is limited by many practical constraints (e.g., instrument capability, nonideal open- and short-connections, etc.). The layer port configuration of the MLM model is similar to a physical multiport planar magnetic structure, it can be analyzed and simulated similar to many experimental measurements (e.g., open- and short-circuit tests), while many practical constraints are avoided. It well captures major electromagnetic interactions and requires few approximations . As a result, by simulating the netlist (i.e., open- and short-circuit tests), one can use the MLM to rapidly extract parameters and generate simpler circuit models, e.g., synthesizing an impedance matrix description as demonstrated in Table II and Fig. 23, or determining self- and mutual-resistances among different windings [9].

V. MODEL VERIFICATION AND APPLICATION EXAMPLES

As part of model verification, the model has been checked against prior known results, including energy storage predictions based on the Poynting's theorem, current distribution at dc, and Dowell's results for series-connected multilayer windings [8]. The check for Poynting's theorem verifies the model with energy conservation rule, and current distribution at dc and the derivation of Dowell's formula can be viewed as special representations of general cases. These theoretical checks examine the MLM model from many different perspectives, and are presented in Appendix II.

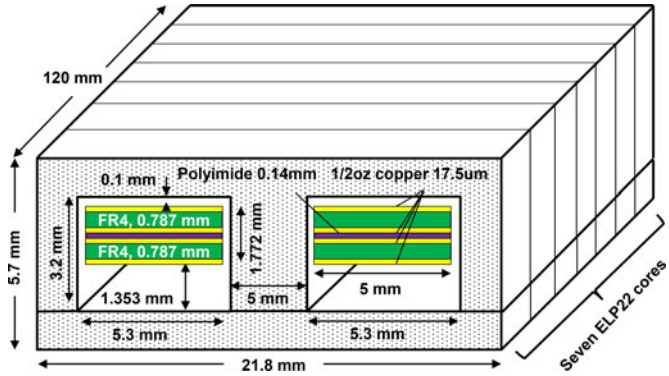

Fig. 9. Geometry of the seven-core four-layer structure. It is used to fabricate the 1:1 and 2:1 transformers. The calculated dc resistance of a single layer at $20\,^{\circ}\mathrm{C}$ is $44.8\,\mathrm{m}\Omega$, which is high enough to be measured with the impedance analyzers.

To further verify the model, we compare the modeling results against FEM simulations and experimental measurements. These verifications also serve as application examples to demonstrate how to use the model in practical designs. Fig. 9 shows the geometry of a selected example structure. It has four one-turn 17-μm-thick (half oz) copper layers, fabricated using two 0.787-mm (31 mil)-thick double-sided copper boards with FR4 material as the core. A 0.14-mm-thick polyimide (Kapton) film is used as the spacing insulator between the two copper boards. Seven ELP22 cores of MnZn ferrite (Epcos N49) are lined up to make a long structure with impedances that were high enough to be accurately measured. Under this setup, since the permeability of the core is very high, the 1-D assumption is satisfied. In all following modeling calculations, μ_0, μ_r, and σ are selected to be $4\pi \times 10^{-7}\ \mathrm{H \cdot m^{-1}}$, 1500, and $5.8 \times 10^{7}\ \mathrm{S \cdot m^{-1}}$, respectively. Cases with fewer cores and shorter length were also checked to study when the feasible range of the 1-D assumption. The frequency range for testing was 10 kHz to 100 MHz. Two impedance analyzers—Agilent 4192A (5 Hz to 13 MHz) and Agilent 4395A (100 kHz to 500 MHz)—are calibrated and utilized to cover this frequency range. The operating temperature was selected to be $20\,^{\circ}\mathrm{C}$. Fig. 10 shows a few pictures of these prototypes. For each group of devices, interleaving patterns can have significant impact on the impedances and current distributions, as does the spacing of the pcb layer stacks. Three types of configurations, which represent a majority of possible interleaving patterns, are prototyped by connecting the four copper layers in three ways.

1) *1:1 transformers with parallel-connected layers:* Two layers are connected in parallel as a one-turn winding, two layers are connected in parallel as another one-turn winding.
2) *2:1 transformers with hybrid-series–parallel-connected layers:* Two layers are connected in series as a two-turn winding, two layers are connected in parallel as a one-turn winding.

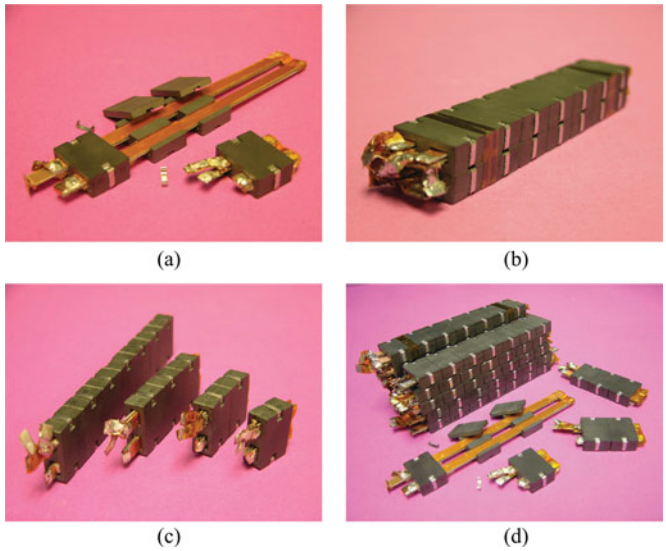

Fig. 10. Photographs of the constructed prototype. (a) Copper layers and magnetic cores of a prototype. (b) Two 2:1 transformers connected and measured in the setup shown in Fig. 11(b). (c) Four 1:1 transformers with different lengths (i.e., one core, two cores, three cores, and seven cores). (d) All constructed prototypes.

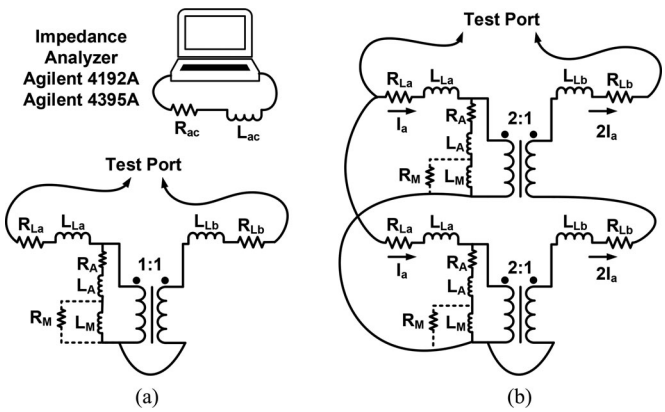

Fig. 11. Experimental configurations for measuring (a) 1:1 transformers with two-parallel-layer pairs; (b) 2:1 transformers with hybrid-series–parallel windings pairs. These configurations avoid exciting the core and, thus, isolate the impact of core losses on the results (bypassing the R_A, L_A, L_M branch). Core loss is not captured in this lumped circuit model. If one would like to include the modeling of core loss, it could be represented as a resistance R_M in parallel with L_M.

3) *One-turn inductors with parallel-connected layers:* Two layers are selected and connected in parallel as a one-turn winding, the other two layers are not presented (this prototype is manufactured using two single-sided copper boards).

The goal is to compare the predicted and measured ac resistance ($R_{\rm ac}$) and ac inductance ($L_{\rm ac}$) in these structures under the setup as shown in Fig. 11 when they are operating in the 10 kHz to 100 MHz frequency range.

A. 1:1 Transformers With Parallel-Connected Layers

Fig. 12 shows three different ways of connecting the four layers in a 1:1 transformer having two paralleled layers in each winding, including one "noninterleaved" option, one "alternating" interleaved option, and one "symmetric" interleaved option. The measurement setup is shown in Fig. 11(a). This setup avoids exciting the magnetizing flux path in the core and, thus, isolates the impact of core losses on the verification results. Cases when the core is excited is separately presented in Section V-C. Fig. 13 shows the lumped circuit models for the four layer structures. Note that in this setup, the impedances associated with the top and bottom magnetic cores (Z_T and Z_B in Fig. 6) carry no flux. Considering cross-layer connections (electrical vias), three simplified circuits shown in Fig. 14 are generated. One can easily analyze these circuits, and compare the $R_{\rm ac}$ and $L_{\rm ac}$ in each case.

In addition, FEM models for these structures are analyzed using the ANSYS Maxwell 2-D FEM simulation package

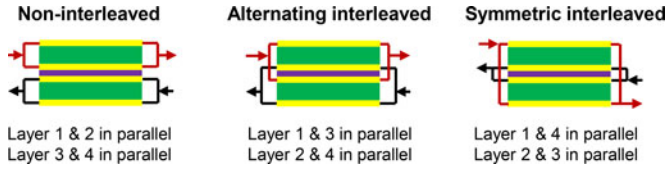

Fig. 12. Three different ways of interleaving the four conductor layers in a 1:1 transformer having two paralleled layers for each winding, including a "noninterleaved" option, an "alternating" interleaved option, and a "symmetric" interleaved option. The four conductive layers are referred as "Layer 1" to "Layer 4" from top to bottom.

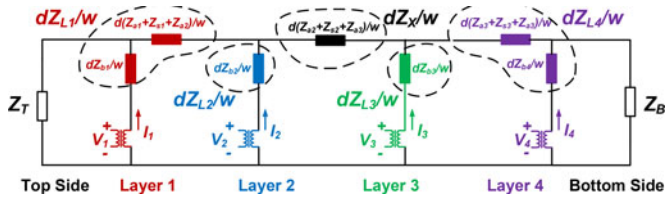

Fig. 13. MLM for the structure shown in Fig. 9 without modeling the electrical vias. The colors of impedances in this figure are labeled in the same way as in Fig. 14.

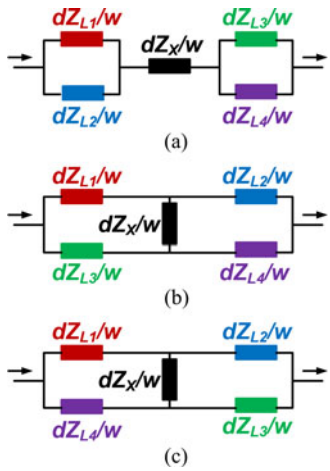

Fig. 14. Simplified MLM for the three interleaving patterns of the 1:1 transformer, including the vias. The colors of impedances in this figure are labeled in the same way as in Fig. 13. Since the core is not excited, the impedances representing the core (Z_T and Z_B) in Fig. 13 have been removed. (a) Noninterleaved. (b) Alternating interleaved. (c) Symmetric interleaved.

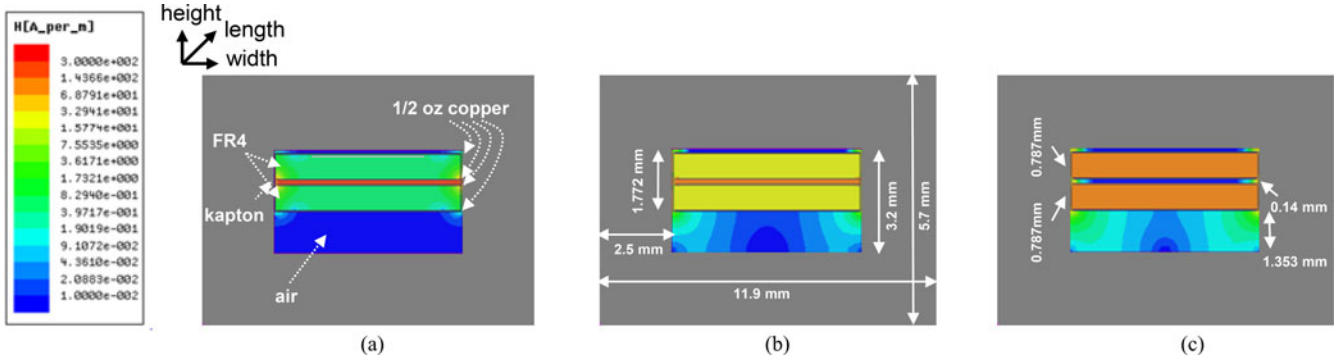

Fig. 15. Magnetic field distribution in three 1:1 transformers having two paralleled layers for each winding, each with different interleaving patterns, driven by a 10 MHz 1-A (peak) current [using the setup in Fig. 11(a)]. Layer indices from top to bottom are layer 1, layer 2, layer 3, layer 4. The simulation was done in ANSYS Maxwell 2-D FEM simulation environment. (a) Noninterleaved. (b) Alternating Interleaved. (c) Symmetric Interleaved.

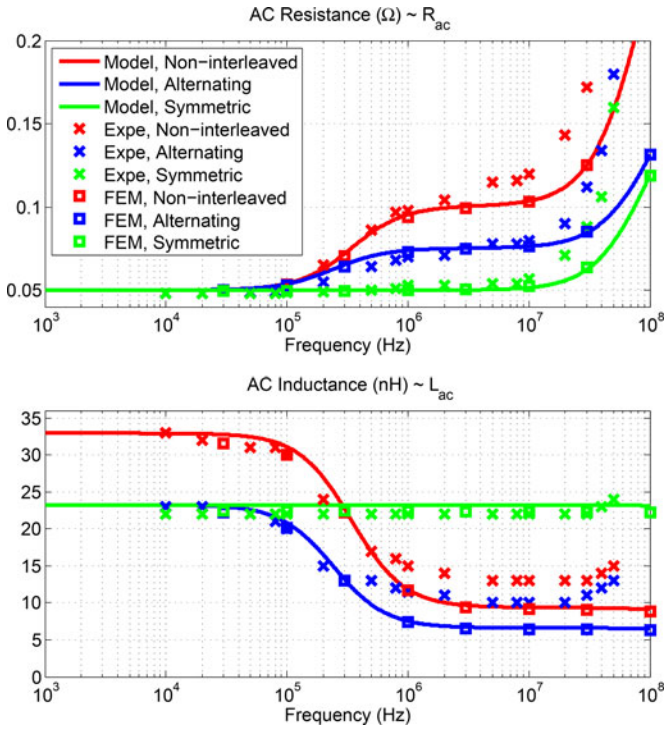

Fig. 16. $R_{\rm ac}$ and $L_{\rm ac}$ of the 1:1 transformer structure with the three interleaving patterns as shown in Fig. 13, predicted by the proposed approach (Model), simulated by ANSYS (FEM), and measured from the prototype (Expe) under the setup as shown in Fig. 11(a).

(version 16.0, 64-bit). Fig. 15 shows the magnetic field strength in the three structures when they are operating at 10 MHz. The dissipated power ($P_{\rm ac}$) and stored reactive energy ($E_{\rm ac}$) in these structures as a function of frequency are found by the software, leading to the simulated $R_{\rm ac}$ and $L_{\rm ac}$ determined by FEM methods. Finally, the ac resistance ($R_{\rm ac}$) and ac inductance ($L_{\rm ac}$) of these transformers are measured with the impedance analyzers using the setup shown in Fig. 11. As shown in Fig. 16, the results from analyzing the lumped circuit model match extremely well with FEM simulations over the entire frequency range,[4] and match very well with experimental measurements. A few practical constraints that may cause the mismatches are investigated in Section VI.

It is known that as the operating frequency increases, skin and proximity effects change the current distribution, changing the real and reactive impedances of a magnetic device. These effects are often extremely difficult to analytically and quantitatively determine when there are parallel layers, multiple windings, and/or multiple interleaving options. The proposed approach is a powerful tool to systematically study and control these complicated frequency-dependent effects. Many qualitative and quantitative findings can be observed from Fig. 16, among those are as follows:

1) Starting from 100 kHz, interleaved designs ("alternating" and "symmetric") have lower loss than the noninterleaved design ("noninterleaved"). The loss reduction can be as high as 50% at 10 MHz.
2) Between the two interleaved structures, the loss of the "symmetric" design can be up to 37.5% lower than that of the "alternating" design at 10 MHz. This is because the current directions in layers 2 and 3 are opposite to each other in the "alternating" design, with narrow spacing in between. A big portion of the current concentrates in layers 2 and 3, causing high loss. This may alternatively be viewed as the "alternating" design having more circulating current in the parallel layers and, hence, higher loss. As the proposed model well predicts this effect, the model is well suited to selecting interleaving configurations (especially when there are parallel layers) to minimize loss.
3) Which interleaving pattern has higher ac resistance actually depends on the pcb layer stack spacings. Fig. 17 shows two selected layer stacks for comparison purposes. One layer stack has thin-polyimide film (0.14 mm) as the middle spacing layer (thin midlayer). This layer stack is also the default layer stack used in this paper. The other layer stack, in comparison, employs a thick FR4 board (1.574 mm) as the middle spacing layer (thick midlayer). The winding width, length, height, core shape, and

[4] This is because ANSYS Maxwell 2-D also made the MQS assumption, and the 1-D assumption is well satisfied in the prototyped geometry. In other words, the FEM software are numerically solving the same Maxwell's equation sets as the proposed analytical model, yield the well-matched results.

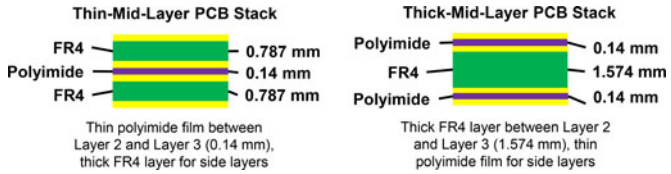

Fig. 17. Two pcb stacks having different spacings among the four conductive layers. (a) Thin midlayer: with thin-polyimide film as the middle spacing layer; (b) Thick midlayer: with thick FR4 board as the middle spacing layer.

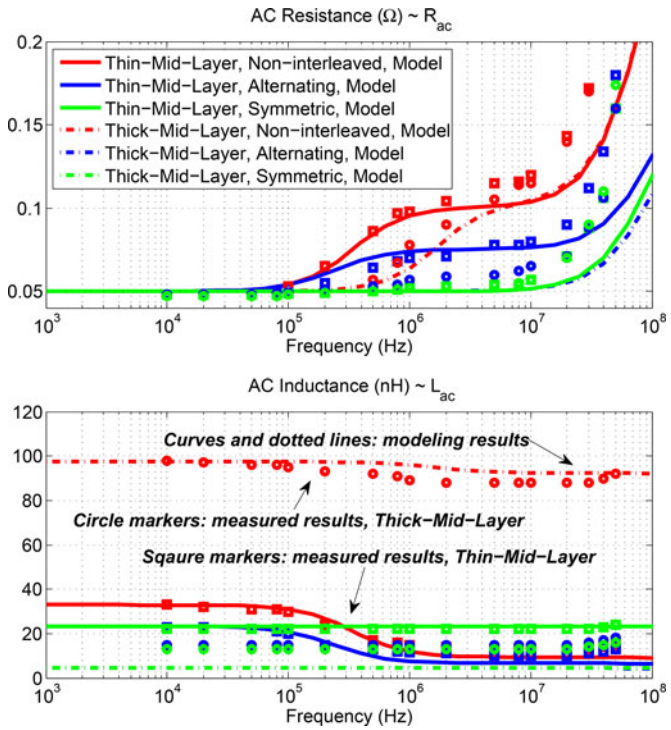

Fig. 18. $R_{\rm ac}$ and $L_{\rm ac}$ of the 1:1 transformer for two different pcb layer stacks and three different interleaving patterns. One layer stack has thin-polyimide film as the middle spacing (thin midlayer). The other layer stack has thick FR4 board as the middle spacing (thick midlayer). Curves and dotted lines are modeling results. Measured results of prototypes with thin midlayer pcb stack spacing are labeled with *square* markers. Measured results of prototypes with thick midlayer pcb stack spacing are labeled with *circle* markers.

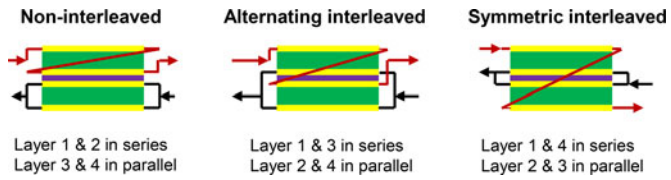

Fig. 19. Three different interleaving patterns of the hybrid-series–parallel 2:1 transformer having one winding comprising two series-connected layers and the other winding comprising two parallel-connected layers.

other experimental aspects are kept the same as described in Fig. 9. The $R_{\rm ac}$ and $L_{\rm ac}$ in the two pcb layer stacks with different interleaving patterns are shown in Fig. 18. With the "thin midlayer" layer stack, the "symmetric" design has significantly lower $R_{\rm ac}$ than the "alternating" design. With the "thick midlayer" layer stack, however, the

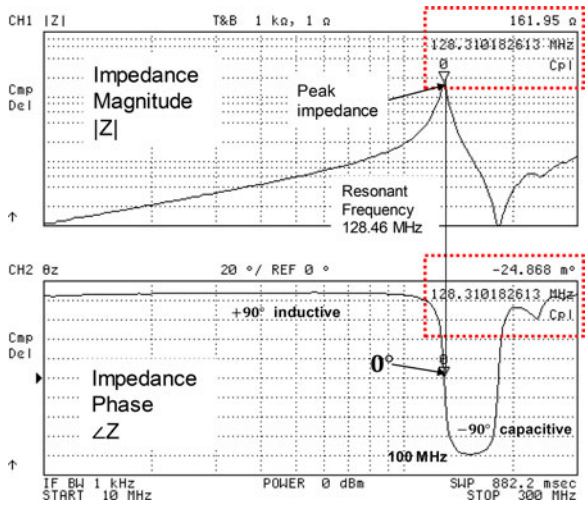

Fig. 20. Measured impedance of the "alternating" interleaved 1:1 transformer [connected as shown in Fig. 11(a), measured using an Agilent 4395A impedance analyzer]. The measured resonant frequency is 128.31 MHz. In comparison, the estimated cross-layer capacitance is 120.04 pF, resulting in an estimated resonant frequency of 162.41 MHz. Many other effects (e.g., interconnects, 2-D effects, 3-D effects, manufacturing mismatches) are not considered in this estimation.

"symmetric" design has slightly higher $R_{\rm ac}$ than the "alternating" design. This example illustrates the importance of considering layer spacing in selecting an interleaving scheme, and demonstrates that the MLM can be used to select the optimal interleaving structure that has the minimum $R_{\rm ac}$ for a chosen pcb stack spacing, and to optimally select pcb stack spacings/materials.

4) The change of the ac resistance is caused by the redistribution of current and magnetic field, which also changes the reactive impedance of the planar structure (e.g., leakage inductances of transformers). The proposed approach can be used to select an interleaving structure that has the most appropriate reactive impedance. As shown in Fig. 18, for the "thin midlayer" layer stack, the "noninterleaved" design has high $L_{\rm ac}$ at low frequencies because it excites high magnetic fields in both the side spacings and the middle spacing. The $L_{\rm ac}$ of the "noninterleaved" design and "alternating" design drop as the frequency increases, because as current concentrates in the middle layers, energy stored in the spacings and within conductors decreases. Considering various interleaving patterns and pcb layer stacks, the proposed approach can be used to model the reactive impedance in a magnetic device, enabling multiple design tradeoffs to be made integrally (e.g., when designing a pcb integrated transformer for an LLC converter).
5) Fig. 20 shows the experimentally measured magnitudes ($|Z|$) and phases ($\angle Z$) of the impedances of the "alternating" interleaved design across the 10–200 MHz range for the configuration shown in Fig. 11(a). The device is inductive when the frequency is lower than 128.31 MHz, and becomes capacitive when the frequency exceeds 128.31 MHz. This threshold frequency is usually referred

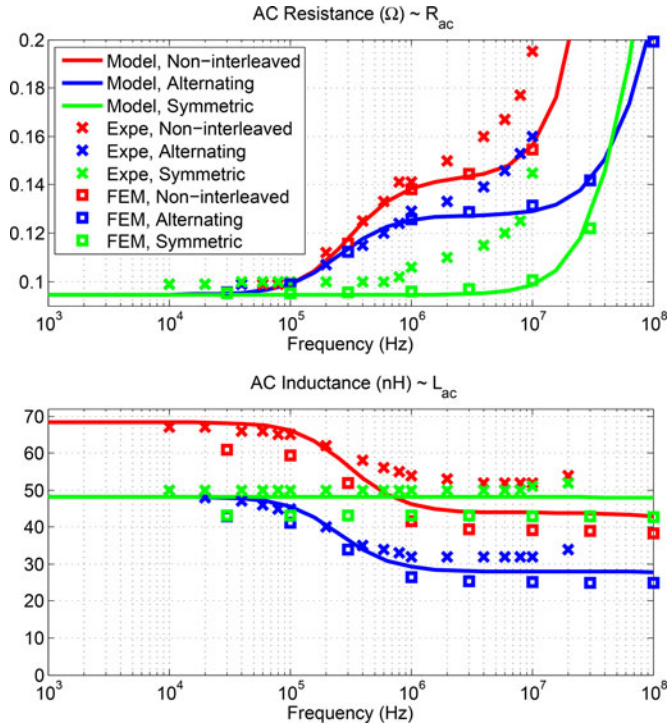

Fig. 21. $R_{\rm ac}$ and $L_{\rm ac}$ of the planar transformer with 2:1 hybrid-series–parallel layers and three interleaving patterns, predicted by the lumped model (labeled as "Model"), simulated by ANSYS (labeled as "FEM"), and measured from the prototype (labeled as "Expe") under the setup as shown in Fig. 11(b).

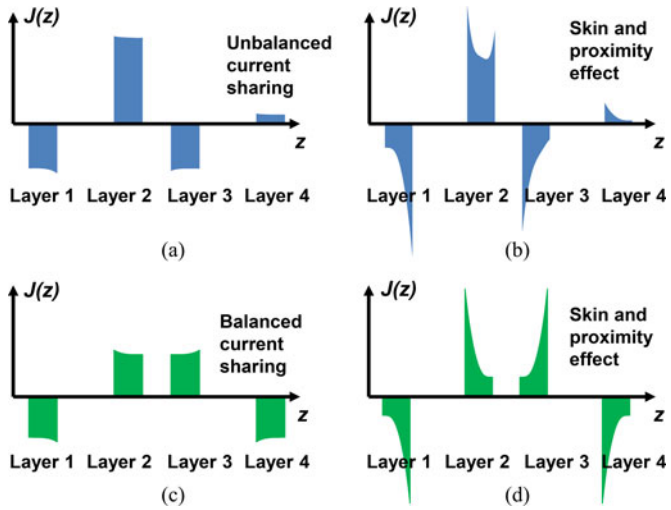

Fig. 22. Calculated current distribution in the four conductive layers in the "alternating" and "symmetric" interleaved transformers under the setup of Fig. 11(b), when they are operating at 10 and 100 MHz, using simplified lumped circuits shown in Fig. 19. The two series-connected layers are shown with negative current densities, while the two parallel-connected layers are shown with positive current densities. (a) Alternating, 10 MHz. (b) Alternating, 100 MHz. (c) Symmetric, 10 MHz. (d) Symmetric, 100 MHz.

to as the "resonant frequency," which is determined by the inductive and capacitive characteristics of the winding layers. As shown in Fig. 16, the modeling/experimental mismatch starts to increase significantly as the frequency approaches the resonant frequency (i.e., frequencies approaching 100 MHz). Under the EQS assumption, the estimated capacitance of the "alternating" interleaved design is 120.04 pF. Following the configuration of Fig. 7, this capacitance is connected in parallel with the estimated ac inductance, resulting in an estimated resonant frequency of 162.41 MHz. Many other effects (e.g., interconnects, 2-D effects, 3-D effects, manufacturing mismatches) which are not considered in this estimation, cause the modeling mismatch. Nevertheless, it can be seen that rough approximation of the resonant frequency (which defines the applicable range of the 1-D MQS model) can be obtained simply by combining the 1-D MQS model with simple EQS models.

B. 2:1 Transformers With Hybrid-Series–Parallel Layers

The purpose of this experiment is to verify the effectiveness of the proposed approach for modeling planar magnetics with hybrid-series- and parallel-connected layers, and to demonstrate more application examples. Fig. 19 shows three different ways one may connect the four layers to construct a 2:1 transformer with both series- and parallel-connected layers. Two layers are series-connected as a two-turn primary winding, and two layers are parallel-connected as a one-turn secondary winding. Because the primary current is twice as large as the secondary current, a "parallel-primary series-secondary" setup as shown in Fig. 11(b) is utilized to measure winding impedances, while avoiding exciting the magnetizing inductance. This setup needs two identical 2:1 transformers. Fig. 21 compares the results from the model, the FEM simulations, and experimental measurements. The modeling results match very well with FEM simulations over the entire frequency range, and match experimental results within 20% up to 10 MHz. This setup has higher mismatch than the 1:1 transformer setup because the two transformers connected to make the measurement are not entirely identical (i.e., exciting the core to the same extent), and the interconnects between the two transformers are not captured in the model. Nevertheless, the results demonstrate the efficacy of the proposed approach for capturing the behavior of sophisticated winding structures.

As a field visualization example, Fig. 22 shows the calculated current distribution (density) within the four layers when the "alternating" and "symmetric" interleaved transformers are operating at 10 and 100 MHz [using (18) after solving the circuit]. Based on this current distribution, the loss of the four layers under the two interleaving connections was calculated and is listed in Table I. Fig. 22 and Table I match with and explain Fig. 21. At 10 MHz, the "symmetric" design has lower $R_{\rm ac}$ than the "alternating" design because its current distributes symmetrically and is equally shared in parallel layers (layers 2 and 4). However, at 100 MHz, with stronger skin and proximity effects, the "alternating" design has lower $R_{\rm ac}$. This is because although current is not equally shared between the two parallel layers in the "alternating" design, its layer 2 is still effectively utilized on both sides, whereas all the layers in the "symmetric" design only carry significant current on one side. At 100 MHz, layer 3 in the "symmetric" design also benefits mildly from carrying

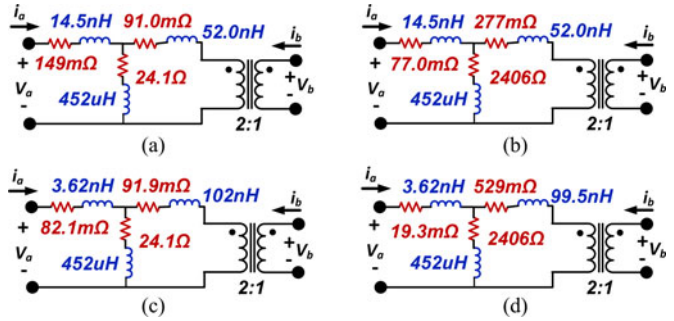

Fig. 23. Simplified circuit models (T models with magnetizing and leakage inductances) of the "alternating" and "symmetric" interleaved transformers when they are operating at 10 and 100 MHz. All component values are extracted from the lumped circuit model by open- and short-circuit simulations. (a) Alternating, 10 MHz. (b) Alternating, 100 MHz. (c) Symmetric, 10 MHz. (d) Symmetric, 100 MHz.

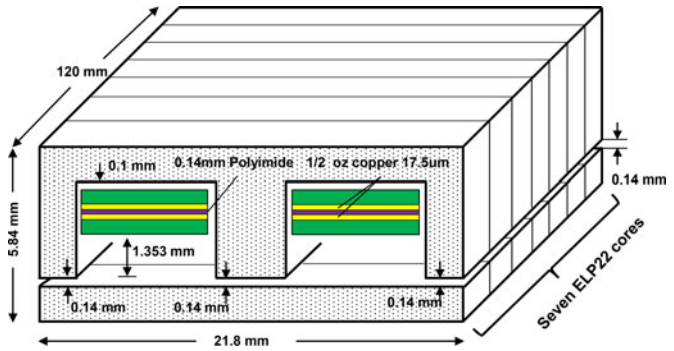

Fig. 24. Geometry of the prototyped two parallel-layer inductor with a narrow spacing between the two conductive layers. Carefully controlled gaps are created in the center and side legs.

current better distributed throughout the conductor, compared to the conductors in the "symmetric" design. It can be concluded that balanced current sharing between parallel-connected layers does not necessarily guarantee lower loss when the frequency is high enough so that the conductor thickness is significant relative to the skin depth. In this frequency range, it is not only the current distribution between layers that matters, but also the current distribution between surfaces of the conductors.

As a parameter extraction example, Table II shows the impedance matrices of the "alternating" and "symmetric" interleaved transformers operating at 10 and 100 MHz. Elements of these impedance matrices are extracted by doing open- and short-circuit simulations using the lumped circuit model in LTspice IV. These impedance matrices are interchangeable with four example simplified circuit models (T models with magnetizing and leakage inductances) as shown in Fig. 23. These simplified circuit models carry the same information as the original MLM model, but have fewer components, can be easily utilized in conventional circuit analysis, and can be easily integrated into circuit simulations. They are related to the models derived in [25], based on short-circuit analysis, but are more complete because they are based on the full impedance matrix (i.e., both the leakage and magnetizing elements are captured under a unified setup).

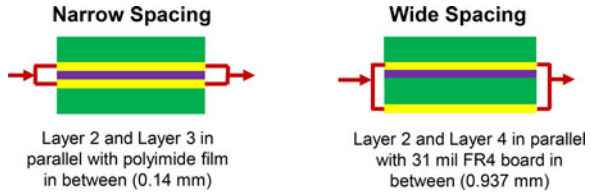

Fig. 25. Two layers out of the four layers are selected and connected in parallel. One implementation has a narrow spacing between the two parallel-connected layers ("Narrow Spacing"). The other implementation has a wide spacing between the two parallel-connected layers ("Wide Spacing").

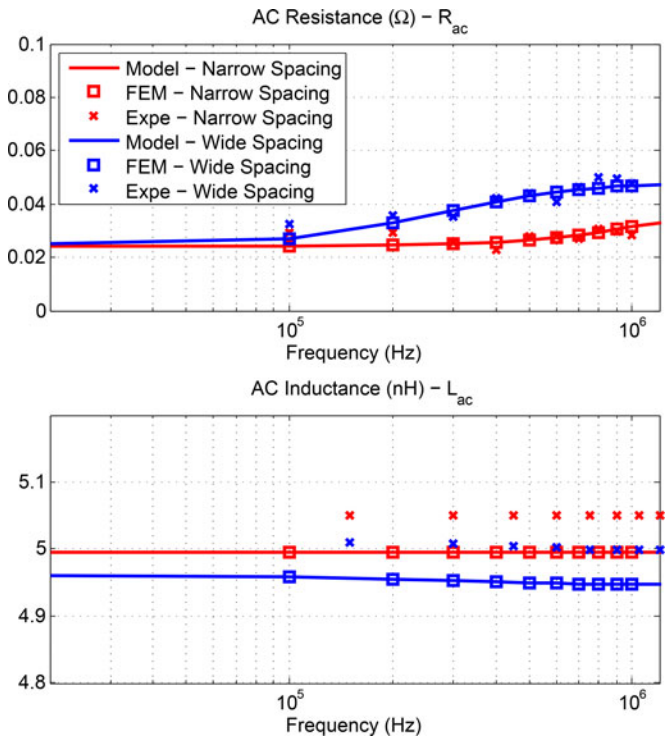

Fig. 26. Comparing the $R_{\rm ac}$ and $L_{\rm ac}$ of the two single-turn inductors shown in Fig. 25 ("Narrow Spacing" and "Wide Spacing") based on the modeling results (Model), FEM simulations (FEM), and experimental measurements (Expe).

Figs. 21–23 and Tables I and II show the same results, and demonstrate a variety of different ways to utilize the model and interpret the results.

C. One-Turn Inductors With Parallel-Connected Layers

The purpose of this experiment is to verify the effectiveness of the proposed approach for modeling planar magnetics with excited cores (e.g., inductors) and parallel-connected layers. (The modeling results for inductors with series-connected layers are theoretically verified by comparing them with Dowell's formulation [8] in Appendix II-C). Figs. 24–25 show the geometry and layer connections of an inductor with two parallel-connected layers. The winding stack is placed far from the air gap to reduce the fringing effect [14], [15]. In one inductor, layers 2 and 3 are selected and paralleled. This inductor has narrow spacing between two layers (polyimide film). In the other

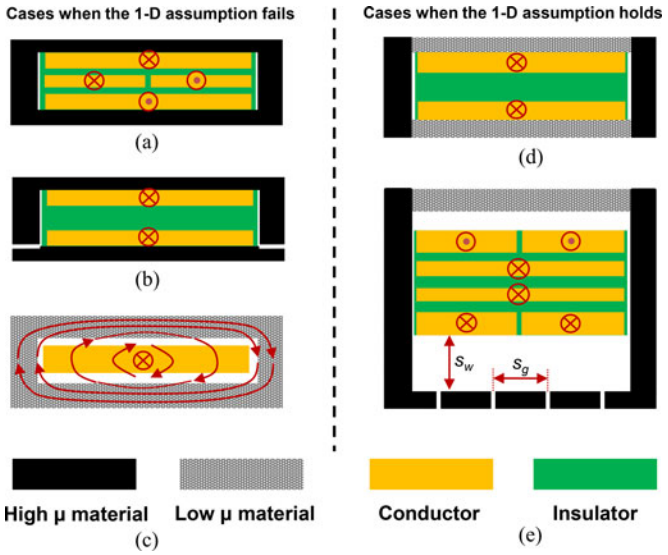

Fig. 27. Example planar structures in which the 1-D assumption (a)–(c) fails, and (d), (e) holds for different reasons.(a) Reason: two winding sections occupy only half of the window breadth each. (b) Reason: the winding stack is located near the air gap. (c) Reason: low permeability material is used as the center leg. (d) Reason: high permeability material is used as the center leg. (e) Reason: gaps are far away from the winding and are well distributed.

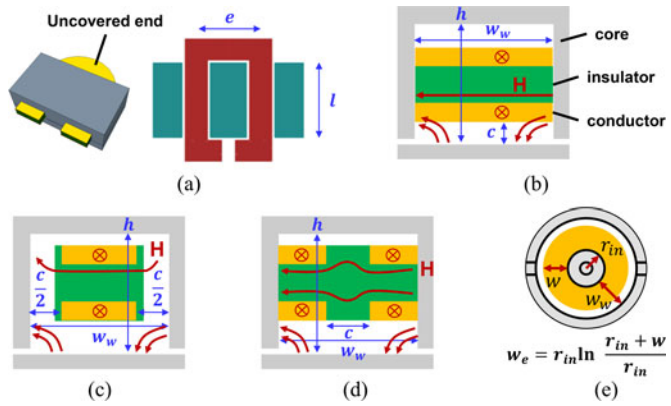

Fig. 28. Five practical constraints that may cause prediction mismatch. (a) End effects. (b) Fringing effects. (c) Conductor to core clearances (side spacing). (d) Conductor to conductor clearances (middle spacing). (e) Radius effects for pot cores.

inductor, layers 2 and 4 are selected and paralleled. This inductor has wide spacing between two layers (FR4 broad and polyimide film). The ac resistance and ac inductance of this inductor are measured with an impedance analyzer (100 kHz to 1 MHz). The core loss can be estimated by using the datasheet, and subtracted to yield the winding loss. At the same time, the $R_{\rm ac}$ and $L_{\rm ac}$ are predicted using the proposed model and FEM simulations. As shown in Fig. 26, the modeling results match very well with FEM results, and match well with experimental results up to 1 MHz (This is the highest recommended operating frequency for the EPCOS N49 MnZn material with known core loss). No effort has been made to measure its core loss above 1 MHz.

VI. Model Applicability and Practical Considerations

A. Model Applicability

The proposed modeling approach predicts accurate results as long as the MQS and 1-D assumptions are both satisfied. In most power electronics applications, the MQS assumption holds because the operating frequency is low enough such that the winding length is much shorter than the corresponding wavelength. The 1-D assumption results in important constraints on applicability. We first provide a general explanation of the situations in which the 1-D assumption applies, followed by empirical examination to better define the boundaries of applicability in practical cases.

High-permeability cores with rectangular winding windows are the most common types of geometries in which the 1-D assumption can, under certain conditions, apply. In a transformer with an ungapped high-permeability core and, thus, negligible magnetizing admittance (high magnetizing inductance), the magnetomotiveforce (MMF) produced by the primary winding is all dropped by the secondary winding(s). If the windings are stacked vertically in a rectangular window, and they all occupy the full breadth of the winding window, the field will be uniform across the breadth of the window, and will only vary with the vertical dimension. In practice, the windings do not truly span the full breadth of the window. There is some spacing for electrical insulation, mechanical support, and/or manufacturing tolerance. Section VI-B.3-4 examines the effect of nonzero spacings in more detail. One example structure that does not satisfy the 1-D assumption but requires special attention is shown in Fig. 27(a). The primary and secondary windings on the middle layer are positioned next to each other horizontally rather than being stacked vertically, resulting in a vertical field component, in addition to the horizontal field component produced by the windings on the bottom and top layers. Thus, the 1-D assumption fails.

Inductors do not satisfy the 1-D assumption as naturally. An air gap in the core will have curved "fringing" flux lines, and if conductors are in this region, the 1-D assumption does not hold [as shown in Fig. 27(b)]. Furthermore, the orientation of the field depends on the position of the gap, even for regions of the window far from the gap. A low-permeability core [as shown in Fig. 27(c)] can be used for an inductor without needing a gap. This might seems to solve the problem and allow the 1-D assumption. However, the result includes concentric field lines near the center of the winding and additional field lines parallel to these further out and closer to the core. These vertical field lines are not captured by the 1-D model.

The most ideal way to achieve a 1-D field in an inductor is to use a composite core with a low-permeability plate on one or two sides of the winding window, and with high-permeability material everywhere else as shown in Fig. 27(d) [60]. This situation can be approximated with multiple distributed gaps in place of the high-permeability material, if the spacing from the winding to the gapped core (s_w) is adequate in comparison to the spacing between the gaps (s_g), as shown in Fig. 27(e), discussed in Section VI-B2 and [14]. With adequate spacing, although the flux distribution in the core region is not 1-D, it is possible to achieve an approximately 1-D field in the winding region with even just one or two gaps.

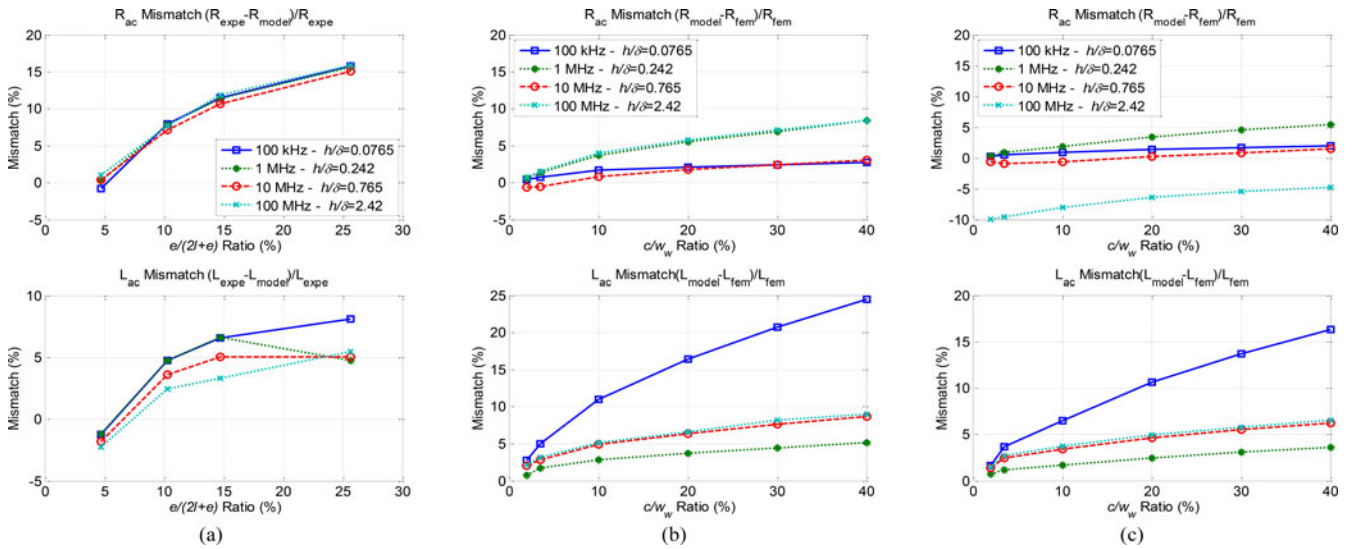

Fig. 29. Mismatch between the modeling results and FEM (or experimental) results when considering (a) end effects (modeling *vs* experimental), (b) conductor-core clearances (modeling *vs* FEM), and (c) conductor-conductor clearances (modeling *vs* FEM). Mismatch is defined as the ratio of the difference between modeling and FEM (or experimental) results. Here h is the thickness of the copper layer (h is default to be half oz, $17.5\ \mu\mathrm{m}$, in this paper), and δ is the skin depth of the conductor depending on the operating frequency. In (b) and (c), since a portion of the conductor width is occupied by spacings, the w used in the model calculation is the modified effective conductor width $w = w_w - c$.

A common misconception is that a short gap length helps us to make the 1-D assumption accurate in an inductor with a gapped core, by minimizing fringing effects. In fact, discrepancies relative to the 1-D approximation are slightly reduced by a longer gap in a sufficiently high-permeability core, as demonstrated in Fig. 7 in [14]. Although a short gap length does mean that the fringing flux is a smaller percentage of the total flux, the strength of the fringing flux for a giving winding current stays approximately constant, independent of gap length, in the region of the winding, if it is spaced well away from the gap. Very close to the gap, the field become more concentrated and causes more severe problems with a shorter gap than with a longer gap.

For transformers with significant magnetizing admittance, deliberately introduced with a gap or the use of a low-permeability core material, the 1-D assumption holds if the winding and gap configurations are both set up according to the considerations above, and are configured to produce field lines in the same axis, such that the one dimension to be analyzed is the same for both.

B. Practical Considerations and Design Rules

Many practical designs may not fully satisfy the 1-D assumption. In some of these cases, the model is still highly accurate, while in others, the error would be unacceptable. Here, we discuss some of these cases along with ways to address them, and present a few rules that can be used to empirically judge the satisfaction of the 1-D assumption. For cases that can be analyzed with 2-D methods, we present the mismatch between the modeling results and FEM simulations. For cases that require 3-D analysis, we present the mismatch between the modeling results and experimental measurements.

1) *End effects:* As shown in Fig. 28(a), in some core shapes, e.g., ELP cores, a portion of the conductor is not covered by the magnetic core. They no longer satisfy the 1-D assumption but require 3-D analysis for full accuracy. We experimentally measured R_{ac} and L_{ac} in four 1:1 transformers with different numbers of cores [as shown in Fig. 10(c)] and compared them with results predicted by the model for different operating conditions. The mismatch as a function of the "uncovered-length to total-length" ratio $(e/(2l+e))$ and the "conductor-thickness to skin-depth" ratio (h/δ) are presented in Fig. 29(a). The mismatch due to end effects does not have a strong dependence on frequency (i.e., h/δ ratio) but is a strong function of the $e/(2l+e)$ ratio. However, in this specific setup, as long as $e/(2l+e)$ is smaller than 25%, the mismatch in R_{ac} is under 15%, and the mismatch in L_{ac} is under 10%. The mismatch can be further reduced by separately calibrating the impedances of the uncovered ends in a way similar to modeling vias and interconnects.
2) *Fringing effects:* As shown in Fig. 28(b), if conductor layers are placed near the air gap, fringing fields can penetrate the windings and change the current distribution, causing modeling mismatches (usually leading to underestimated conduction losses). This effect has been numerically analyzed in [15] and [14], and it was recommended in [14] that the clearance (c) be at least 25% of the total window width w_w (i.e., gap to gap spacing) to limit the fringing effects.
3) *Conductor-core clearances (side spacing):* As shown in Fig. 28(c), clearances are required between conductors and pcb edges, and between pcb edges and the core. These clearances change the dissipated loss and stored reactive energy from a 2-D perspective. Fig. 29(b) shows the

mismatch between the model prediction and FEM results as a function of the "clearance to window-width" ratio (c/w_w), and the "conductor-thickness to skin-depth" ratio (h/δ) for the 1:1 transformers described in Section V-A. Up to frequencies where h/δ equals 2.42 (this frequency is 100 MHz for half-oz copper), the mismatch of $R_{\rm ac}$ is less than 10% if c/w_w is smaller than 40%. For accurate estimation of $L_{\rm ac}$, it is preferable if h/δ is below 1. Note, for half-oz copper ($17.5\,\mu$m), the frequency when h/δ equals 1 is approximately 14 MHz, similar results are found in [63].

4) *Conductor–conductor clearances (middle spacing):* As shown in Fig. 28(d), clearances between two adjacent turns can also cause mismatches. Fig. 29(c) shows the increase in mismatch as the c/w_w ratio increases. Up to frequencies when h/δ equals 2.42, the mismatch in $R_{\rm ac}$ is less than 10% if c/w_w is smaller than 40%. To achieve accurate estimation for $L_{\rm ac}$, it is preferable if h/δ is below 1.
5) *Radius effects for pot cores:* Fig. 28(e) shows a pot core whose window width (w_w) is comparable to its window inner radius ($r_{\rm in}$). In this situation, the magnetic field and current distributions along with the radius follows a "logarithmic" distribution similar to that described in [10] and [42]. Assuming that the conductive layer fills the window width (i.e., $w = w_w$), this effect can be easily included in the lumped circuit model by replacing the layer width (w) in all impedance calculations with an effective width $w_e = r_{\rm in}\ln(1+\frac{w}{r_{\rm in}})$ (Note: $\lim_{r_{\rm in}\to+\infty} w_e = w$).

VII. Conclusion

This paper presents a systematic approach to modeling impedances and current distribution in planar magnetics. The electromagnetic interactions in planar magnetics are clarified, organized, and converted into a lumped circuit model under the 1-D and MQS assumptions. The lumped circuit model can be used to estimate the ac impedances, to determine current sharing in parallel windings, and to extract parameters for impedance matrices and simplified circuit models, among many other uses. The proposed approach is tied with and verified by many existing theories, reexamining them from new perspectives and revealing their relationships. The modeling performance under a few practical constraints is investigated experimentally to clarify the boundaries of applicability. It is demonstrated that the approach performs very well in modeling commonly used planar magnetics.

Appendix I
Derivation of the Lumped Circuit Model

This appendix derives the lumped circuit model in detail. All variables are the same as those utilized in Section III.

A. Modeling a One-Turn Layer

Under the 1-D approximation, the magnetic field within a conductive layer satisfies the 1-D diffusion equation [48]

$$\frac{1}{\mu\sigma}\nabla^2 H_x = \frac{dH_x}{dt}. \tag{20}$$

Its solution is

$$H_x(z) = \frac{[H_T\sinh(\Psi z) + H_B\sinh(\Psi(h-z))]}{\sinh(\Psi h)}. \tag{21}$$

Here, $\Psi = \frac{1+j}{\delta}$, $\delta = \sqrt{\frac{2}{\omega\mu_r\mu_0\sigma}}$. Using *Ampere's law* under the MQS approximation: $\nabla\times H_x(z) = J_y(z) = \sigma E_y(z)$, gives

$$E_y(z) = \frac{\Psi}{\sigma}\left[\frac{H_T e^{\Psi h} - H_B}{e^{\Psi h} - e^{-\Psi h}}e^{-\Psi(h-z)} - \frac{H_B e^{\Psi h} - H_T}{e^{\Psi h} - e^{-\Psi h}}e^{-\Psi z}\right]. \tag{22}$$

At the top and bottom surface of the conductor (i.e., when $z = 0$ and $z = h$), (24) gives

$$\begin{aligned} E_T = E_y(h) &= \frac{\Psi}{\sigma}\left[\frac{H_T e^{\Psi h} - H_B}{e^{\Psi h} - e^{-\Psi h}} - \frac{H_B - H_T e^{-\Psi h}}{e^{\Psi h} - e^{-\Psi h}}\right] \\ E_B = E_y(0) &= \frac{\Psi}{\sigma}\left[\frac{H_T - H_B e^{-\Psi h}}{e^{\Psi h} - e^{-\Psi h}} - \frac{H_B e^{\Psi h} - H_T}{e^{\Psi h} - e^{-\Psi h}}\right]. \end{aligned} \tag{23}$$

Defining impedance Z_a and Z_b as

$$\begin{aligned} Z_a &= \frac{\Psi(1-e^{-\Psi h})}{\sigma(1+e^{-\Psi h})} \\ Z_b &= \frac{2\Psi e^{-\Psi h}}{\sigma(1-e^{-2\Psi h})} \end{aligned} \tag{24}$$

allows (25) to be simplified to

$$\begin{aligned} E_T &= Z_a H_T + Z_b(H_T - H_B) \\ E_B &= Z_b(H_T - H_B) - Z_a H_B. \end{aligned} \tag{25}$$

Also by *Ampere's law*

$$(H_T - H_B)w = I = Kw \tag{26}$$

combining (25) and (26), we get

$$\begin{aligned} E_T &= Z_a H_T + Z_b K \\ E_B &= Z_b K - Z_a H_B. \end{aligned} \tag{27}$$

This yields (1) and (3) in Section III-A.

B. Modeling Two Adjacent One-Turn Layers

In Fig. 3(a), consider a closed loop surrounding the center post that includes the bottom surface of layer 1 and the external voltage source V_1. Applying *Faraday's law* to the loop gives

$$E_{B1}d - V_1 = -\frac{d\Phi_{B1}}{dt} \tag{28}$$

where Φ_{B1} is the magnetic flux in the center post across the bottom surface of layer 1. Similarly, consider a closed loop surrounding the center post that includes the top surface of layer 2 and the external voltage source V_2

$$E_{T2}d - V_2 = -\frac{d\Phi_{T2}}{dt} \tag{29}$$

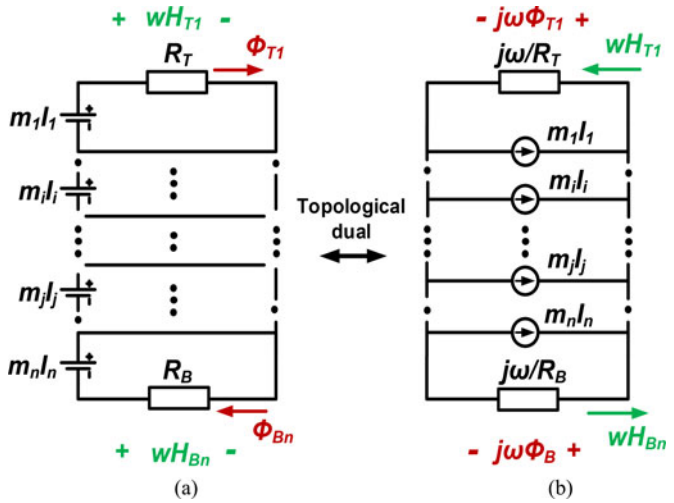

Fig. 30. Magnetic reluctance circuit model of a planar structure with (a) MMFs modeled as voltage sources, and (b) its topological dual with MMFs modeled as current sources. All reluctance values are replaced by the time derivative of the corresponding permeances ($j\omega\frac{1}{\mathcal{R}}$). If complex reluctances are used, the core loss is naturally captured by the model. Fig. 30(b) can be merged with Fig. 4(b) becoming Fig. 6, with across ($j\omega\Phi$) and through (wH) variables mapped one-by-one with each other.

where Φ_{T2} is the magnetic flux in the center post across the top surface of layer 2. Now, the magnetic flux penetrating into the center post through the spacing between the two layers (Φ_{S12}), equals $\mu_0 a_1 dH_{S12}$. Using flux continuity, $\Phi_{T2} = \Phi_{B1} + \Phi_{S12}$, and taking the derivative gives

$$\frac{d\Phi_{T2}}{dt} = \frac{d\Phi_{B1}}{dt} + \frac{d\Phi_{S12}}{dt}. \tag{30}$$

Combining (28)–(30) gives

$$H_{S12} = \frac{1}{j\omega\mu_0 a_1}\left(\frac{V_2}{d} - E_{T2} - \frac{V_1}{d} + E_{B1}\right). \tag{31}$$

This yields (8) in Section III-B.

C. Modeling the Magnetic Core and the Air Gaps

The modeling of the magnetic core and air gaps in the MLM approach was derived directly using Maxwell's equations in our earlier conference paper [52]. Here, we present a more generally applicable derivation closely related to the conventional magnetic reluctance circuit model, to highlight a different way of interpreting this model, and to tie this study with other reluctance-based core models, especially the Gyrator-capacitor approaches, which utilize the concept of magnetic and electrical circuit duality [61], [62]. This derivation also releases the requirement of 1-D field distribution from the core region, leaving the 1-D assumption only required in the winding region.

Assuming $\mathcal{R}_T$ is the reluctance of the top side of the core, and $\mathcal{R}_B$ is the reluctance of the bottom side of the core, a magnetic circuit model as shown in Fig. 30(a) can be generated. This model captures the electromagnetic interactions related the core, but does not capture those in the windings. To make this model compatible with the modeling of the winding stack, we take the topological dual of this circuit by modeling the MMF generators as current sources and taking the time derivative of all permeances ($j\omega\frac{1}{\mathcal{R}}$), as shown in Fig. 30(b). This circuit, which models the core and the air gaps, can be merged with the circuit in Fig. 4(b) (using n modular impedance networks to model n layers), which captures the conductors and spacings, with all across ($j\omega\Phi$) and through (wH) variables mapped one-by-one with each other. The merged circuit contains all information and is shown in Fig. 6. Specifically, Φ_{T1} is the magnetic flux carried by the top side of the core; Φ_{B1} is the magnetic flux carried by the bottom side of the core; wH_{T1} equals the integral of the H field strength along with any trace through the top side of the magnetic core; wH_{Bn} equals the integral of the H field strength along any trace through the bottom side of the magnetic core. By relating the E, V, Φ, H, and $\mathcal{R}$

$$\begin{aligned} dE_{T1} - \frac{V_1}{m_1} &= -j\omega\Phi_{T1} = -\frac{j\omega}{\mathcal{R}_T} wH_{T1} \\ dE_{Bn} - \frac{V_n}{m_n} &= -j\omega\Phi_{Bn} = \frac{j\omega}{\mathcal{R}_B} wH_{Bn}. \end{aligned} \tag{32}$$

This yields (11) in Section III-C.

Appendix II
Theoretical Verifications

The proposed modeling approach can be theoretically verified by checking its results against some known results.

A. Poynting's Theorem and Energy Conservation Rule

The energy processed in any structure must satisfy the Poynting's theorem; the power dissipated and stored within it must equal the integral of the Poynting vector over a closed surface boundary cutting into this surface. In Fig. 4(a), assuming that there is no spacing between two series-connected turns on the same layer, and that all turns have the same width $\frac{w}{m_1}$, the complex power dissipated and stored in layer 1 is

$$P_{\text{poynting}} = \underbrace{dw}_{\text{Surface Area}} \underbrace{(E_{T1}H_{T1}^* - E_{B1}H_{B1}^*)}_{\text{Poynting vectors}}. \tag{33}$$

Now, consider the three-terminal impedance network of "Layer 1" in Fig. 4(b). The electrical power going into layer 1 is

$$\begin{aligned} P_{\text{model}} = & \\ & \underbrace{\frac{V_1}{m_1} m_1 I_1^* + \left(\frac{V_1}{m_1} - E_{B1}d\right) wH_{B1}^* - \left(\frac{V_1}{m_1} - E_{T1}d\right) wH_{T1}^*}_{\text{Electrical power of the three terminals}} \\ & = dw(E_{T1}H_{T1}^* - E_{B1}H_{B1}^*). \end{aligned} \tag{34}$$

Hence, the match between (33) and (34) shows that the MLM model predicts the same loss and energy storage in a layer as the Poynting's theorem. The energy conservation rule holds.

B. Current Distribution at DC

The proposed modeling approach can be checked to ensure that it predicts correct results in the extreme case when the conductor carries dc current ($\omega \to 0$). For the one-turn layer shown in Fig. 2, if $\omega \to 0$, then $\delta \to \infty$, and $\Psi \to 0$. Using (18), the current distribution at dc is

$$\lim_{\Psi\to 0} J_y(z) = \lim_{\Psi\to 0} \frac{2(H_T - H_B)\Psi}{e^{\Psi h} - e^{-\Psi h}} = \frac{K}{h}. \tag{35}$$

This indicates that the current distribution is a constant along the conductor thickness when $\omega \to 0$, which is as expected.

C. Dowell's Formulation

For planar structures with multiple adjacent layers connected in series, the proposed approach can be used to derive the well-known Dowell's formulation [8]. Considering the planar structure shown in Figs. 5 and 6, if all n layers are one-turn layers with identical thicknesses h and width w, and all n layers are connected in series, the ac impedance of this n layer structure is

$$Z_{\rm ac} = \left(nZ_b + 2Z_a \sum_{k=1}^{n-1} k^2 + n^2 Z_a \right). \tag{36}$$

Substituting (14) into (36), the ac resistance ($R_{\rm ac}$) can be found as the real part of $Z_{\rm ac}$

$$\begin{aligned} R_{\rm ac} = \Re(Z_{\rm ac}) = R_{\rm dc}\Delta \times \Re\left[\coth(\Delta(1+i))(1+i)\right] \\ + R_{\rm dc}\frac{2(n^2-1)}{3}\Delta \times \Re\left[\tanh\left(\frac{\Delta}{2}(1+i)\right)(1+i)\right]. \end{aligned} \tag{37}$$

Here, $R_{\rm dc} = \frac{nd}{\sigma wh}$ and is the dc resistance of the n series layers. Δ is the "thickness-to-skin-depth" ratio ($\frac{h}{\delta}$). Since

$$\begin{aligned} \Re\left[\coth(\Delta(1+i))(1+i)\right] &= \frac{\sinh(2\Delta)+\sin(2\Delta)}{\cosh(2\Delta)-\cos(2\Delta)} \\ \Re\left[\tanh(\frac{\Delta}{2}(1+i))(1+i)\right] &= \frac{\sinh(\Delta)-\sin(\Delta)}{\cosh(\Delta)+\cos(\Delta)} \end{aligned} \tag{38}$$

the ac resistance to dc resistance ratio, $F_R = \frac{R_{\rm ac}}{R_{\rm dc}}$, is

$$\begin{aligned} F_R = \Delta\Bigg(&\frac{\sinh(2\Delta)+\sin(2\Delta)}{\cosh(2\Delta)-\cos(2\Delta)} \\ &+ \frac{2(n^2-1)}{3}\frac{\sinh(\Delta)-\sin(\Delta)}{\cosh(\Delta)+\cos(\Delta)}\Bigg). \end{aligned} \tag{39}$$

This is the well-known Dowell's formulation.

REFERENCES

[1] A. M. Urling, V. A. Niemela, G. R. Skutt, and T. G. Wilson, "Characterizing high-frequency effects in transformer windings—A guide to several significant articles," in *Proc. IEEE Appl. Power Electron. Conf. Expo.*, Mar. 13–17, 1989, pp. 373–385.

[2] M. T. Quirke, J. J. Barrett, and M. Hayes, "Planar magnetic component technology—A review," *IEEE Trans. Compon. Hybrids, Manuf. Technol.*, vol. 15, no. 5, pp. 884–892, Oct. 1992.

[3] N. Dai, A. W. Lofti, G. Skutt, W. Tabisz, and F.C. Lee, "A comparative study of high-frequency, low-profile planar transformer technologies," in *Proc. IEEE Appl. Power Electron. Conf. Expo.*, Feb. 1994, vol. 1, pp. 226–232.

[4] Z. Ouyang and M. Andersen, "Overview of planar magnetic technology—Fundamental properties," *IEEE Trans. Power Electron.*, vol. 29, no. 9, pp. 4888–4900, Sep. 2014.

[5] D. J. Perreault, J. Hu, J. M. Rivas, Y. Han, O. Leitermann, R. C. N. Pilawa-Podgurski, A. Sagneri, and C. R. Sullivan, "Opportunities and challenges in very high frequency power conversion," in *Proc. IEEE Appl. Power Electron. Conf. Expo.*, Feb. 2009, pp. 1–14.

[6] C. R. Sullivan, D. V. Harburg, J. Qiu, C. G. Levey, and D. Yao, "Integrating magnetics for on-chip power: A perspective," *IEEE Trans. Power Electron.*, vol. 28, no. 9, pp. 4342–4353, Sep. 2013.

[7] M. Araghchini, J. Chen, V. Doan-Nguyen, D. V. Harburg, D. Jin, J. Kim, M. S. Kim, S. Lim, B. Lu, D. Piedra, J. Qiu, J. Ranson, M. Sun, X. Yu, H. Yun, M. G. Allen, J. A. del Alamo, G. DesGroseilliers, F. Herrault, J. H. Lang, C. G. Levey, C. B. Murray, D. Otten, T. Palacios, D. J. Perreault, and C. R. Sullivan, "A technology overview of the powerchip development program," *IEEE Trans. Power Electron.*, vol. 28, no. 9, pp. 4182–4201, Sep. 2013.

[8] P. L. Dowell, "Effects of eddy currents in transformer windings," *Proc. Inst. Electr. Eng.*, vol. 113, no. 8, pp. 1387–1394, Aug. 1966.

[9] J. H. Spreen, "Electrical terminal representation of conductor loss in transformers," *IEEE Trans. Power Electron.*, vol. 5, no. 4, pp. 424–429, Oct. 1990.

[10] W. G. Hurley and M. C. Duffy, "Calculation of self and mutual impedances in planar magnetic structures," *IEEE Trans. Magn.*, vol. 31, no. 4, pp. 2416–2422, Jul. 1995.

[11] W. G. Hurley, E. Gath, and J. G. Breslin, "Optimizing the AC resistance of multilayer transformer windings with arbitrary current waveforms," *IEEE Trans. Power Electron.*, vol. 15, no. 2, pp. 369–376, Mar. 2000.

[12] J.-P. Vandelac and P. D. Ziogas, "A novel approach for minimizing high-frequency transformer copper losses," *IEEE Trans. Power Electron.*, vol. 3, no. 3, pp. 266–277, Jul. 1988.

[13] C. R. Sullivan, "Computationally efficient winding loss calculation with multiple windings, arbitrary waveforms, and two-dimensional or three-dimensional field geometry," *IEEE Trans. Power Electron.*, vol. 16, no. 1, pp. 142–150, Jan. 2001.

[14] J. Hu and C. R. Sullivan, "AC resistance of planar power inductors and the quasidistributed gap technique," *IEEE Trans. Power Electron.*, vol. 16, no. 4, pp. 558–567, Jul. 2001.

[15] A. F. Goldberg, J. G. Kassakian, and M. F. Schlecht, "Issues related to 1–10-MHz transformer design," *IEEE Trans. Power Electron.*, vol. 4, no. 1, pp. 113–123, Jan. 1989.

[16] A. F. Goldberg and M. F. Schlecht, "The relationship between size and dissipated power in a 1–10 MHz transformer," *IEEE Trans. Power Electron.*, vol. 7, no. 1, pp. 63–74, Jan. 1992.

[17] E. Santi and S. Cuk, "Accurate leakage models of gapped magnetic circuits," in *Proc. IEEE Appl. Power Electron. Conf. Expo.*, Mar. 7–11, 1993, pp. 596–603.

[18] C. P. Steinmetz, "On the law of hysteresis," *Proc. IEEE*, vol. 72, no. 2, pp. 197–221, Feb. 1984.

[19] J. H. Chan, A.Vladimirescu, X.-C. Gao, P. Liebmann, and J. Valainis, "Nonlinear transformer model for circuit simulation," *IEEE Trans. Comput.-Aided Des. Integr. Circuits Syst.*, vol. 10, no. 4, pp. 476–482, Apr. 1991.

[20] W.-J. Gu and R. Liu, "A study of volume and weight vs. frequency for high-frequency transformers," in *Proc. IEEE Power Electron. Spec. Conf.*, Jun. 20–24, 1993, pp. 1123–1129.

[21] J. Li, T. Abdallah, and C. R. Sullivan, "Improved calculation of core loss with nonsinusoidal waveforms," in *Proc. IEEE Annu. Meet. Ind. Appl. Soc.*, Sep. 2001, vol. 4, pp. 2203–2210.

[22] K. Venkatachalam, C. R. Sullivan, T. Abdallah, and H. Tacca, "Accurate prediction of ferrite core loss with nonsinusoidal waveforms using only Steinmetz parameters," in *Proc. IEEE Workshop Comput. Power Electron.*, Jun. 3–4, 2002, pp. 36–41.

[23] J. Muhlethaler, J. Biela, J. W. Kolar, and A. Ecklebe, "Core losses under the DC bias condition based on Steinmetz parameters," *IEEE Trans. Power Electron.*, vol. 27, no. 2, pp. 953–963, Feb. 2012.

[24] Y. Han, G. Cheung, A. Li, C. R. Sullivan, and D. J. Perreault, "Evaluation of magnetic materials for very high frequency power applications," *IEEE Trans. Power Electron.*, vol. 27, no. 1, pp. 425–435, Jan. 2012.

[25] V. A. Niemela, G. R. Skutt, A. M. Urling, Y.-N. Chang, T. G. Wilson, Jr., H. A. Owen, and R. C. Wong, "Calculating the short-circuit impedances of a multiwinding transformer from its geometry," in *Proc. IEEE Power Electron. Spec. Conf.*, Jun. 26–29, 1989, vol. 2, pp. 607–617.

[26] R. W. Erickson and D. Maksimovic, "A multiple-winding magnetics model having directly measurable parameters," in *Proc. IEEE Power Electron. Spec. Conf.*, May 17–22, 1998, vol. 2, pp. 1472–1478.

[27] W. Chen, Y. Yan, Y. Hu, and Q. Lu, "Model and design of PCB parallel winding for planar transformer," *IEEE Trans. Magn.*, vol. 39, no. 5, pp. 3202–3204, Sep. 2003.

[28] J. G. Hayes, N. O'Donovan, and M. G. Egan, "The extended T model of the multiwinding transformer," in *Proc. IEEE Power Electron. Spec. Conf.*, Jun. 20–25, 2004, vol. 3, pp. 1812–1817.

[29] J. D. Jr, van Wyk, W. A. Cronje, J. D. van Wyk, C. K. Campbell, and P. J. Wolmarans, "Power electronic interconnects: Skin- and proximity-effect-based frequency selective-multipath propagation," *IEEE Trans. Power Electron.*, vol. 20, no. 3, pp. 600–610, May 2005.

[30] D. Fu, F. C. Lee, and S. Wang, "Investigation on transformer design of high frequency high efficiency dc-dc converters," in *Proc. IEEE Appl. Power Electron. Conf. Expo.*, Feb. 21–25, 2010, pp. 940–947.

[31] Z. Ouyang, O. C. Thomsen, and M. Andersen, "Optimal design and tradeoff analysis of planar transformer in high-power DCDC converters," *IEEE Trans. Ind. Electron.*, vol. 59, no. 7, pp. 2800–2810, Jul. 2012.

[32] J.-P. Keradec, B. Cogitore, and F. Blache, "Power transfer in a two-winding transformer: From 1-D propagation to an equivalent circuit," *IEEE Trans. Magn.*, vol. 32, no. 1, pp. 274–280, Jan. 1996.
[33] A. Schellmanns, P. Fouassier, J.-P. Keradec, and J.-L. Schanen, "Equivalent circuits for transformers based on one-dimensional propagation: Accounting for multilayer structure of windings and ferrite losses," *IEEE Trans. Magn.*, vol. 36, no. 5, pp. 3778–3784, Sep. 2000.
[34] A. Schellmanns, K. Berrouche, and J.-P. Keradec, "Multiwinding transformers: A successive refinement method to characterize a general equivalent circuit," *IEEE Trans. Instrum. Meas.*, vol. 47, no. 5, pp. 1316–1321, Oct. 1998.
[35] X. Margueron and J.-P. Keradec, "Design of equivalent circuits and characterization strategy for n-input coupled inductors," *IEEE Trans. Ind. Appl.*, vol. 43, no. 1, pp. 14–22, Jan./Feb. 2007.
[36] X. Margueron, A. Besri, Y. Lembeye, and J.-P. Keradec, "Current sharing between parallel turns of a planar transformer: Prediction and improvement using a circuit simulation software," *IEEE Trans. Ind. Appl.*, vol. 46, no. 3, pp. 1064–1071, May/Jun. 2010.
[37] J. M. Lopera, M. Pernia, J. Diaz, J. M. Alonso, and F. Nuno, "A complete transformer electric model, including frequency and geometry effects," in *Proc. IEEE Power Electron. Spec. Conf.*, Jun. 1992, vol. 2, pp. 1247–1252.
[38] A. M. Pernia, F. Nuno, and J. M. Lopera, "Magnetic elements simulation in power converters," in *Proc. Tech. Int. Power Electron. Congr.*, Aug. 21–25, 1994, pp. 74–79.
[39] A. M. Pernia, F. Nuno, and J. M. Lopera, "1D/2D transformer electric model for simulation in power converters," in *Proc. IEEE Power Electron. Spec. Conf.*, Jun. 18–22, 1995, vol. 2, pp. 1043–1049.
[40] R. Prieto, J. A. Cobos, O. Garcia, P. Alou, and J. Uceda, "Using parallel windings in planar magnetic components," in *Proc. IEEE Power Electron. Spec. Conf.*, 2001, vol. 4, pp. 2055–2060.
[41] J. M. Lopera, M. J. Prieto, A. M. Perna, and F. N. Nuno, "A multiwinding modeling method for high frequency transformers and inductors," *IEEE Trans. Power Electron.*, vol. 18, no. 3, pp. 896–906, May 2003.
[42] R. Prieto, J. A. Oliver, J. A. Cobos, and M. Christini, "Magnetic component model for planar structures based on transmission lines," *IEEE Trans. Ind. Electron.*, vol. 57, no. 5, pp. 1663–1669, May 2010.
[43] A. F. Goldberg, J. G. Kassakian, and M. F. Schlecht, "Finite-element analysis of copper loss in 1–10 MHz transformers," *IEEE Trans. Power Electron.*, vol. 4, no. 2, pp. 157–167, Apr. 1989.
[44] M. J. DeBortoli, S. J. Salon, D. W. Burow, and C. J. Slavik, "Effects of rotor eccentricity and parallel windings on induction machine behavior: A study using finite element analysis," *IEEE Trans. Magn.*, vol. 29, no. 2, pp. 1676–1682, Mar. 1993.
[45] R. Asensi, R. Prieto, J. A. Cobos, and J. Uceda, "Modeling high-frequency multiwinding magnetic components using finite-element analysis," *IEEE Trans. Magn.*, vol. 43, no. 10, pp. 3840–3850, Oct. 2007.
[46] N. Y. Abed and O. A. Mohammed, "Physics-based high-frequency transformer modeling by finite elements, *IEEE Trans. Magn.*, vol. 46, no. 8, pp. 3249–3252, Aug. 2010.
[47] MIT EE Staff, "Transformers; General principles," in *Magnetic Circuits and Transformers.* Cambridge, MA, USA: MIT Press, 1943.
[48] H. A. Haus and J. R. Melcher, "Introduction to electroquasistatics and magnetoquasistatics," in *Electromagnetic Fields and Energy.*, Englewood Cliffs, NJ, USA: Prentice-Hall, 1989.
[49] J. G. Kassakian, M. F. Schlecht, and G. C. Verghese, "Magnetic components, " in, *Principles of Power Electronics*. Reading, MA, USA: Addison-Wesley, 1991.
[50] P. T. Krein, "Concepts of magnetics for power electronics," in *Elements of Power Electronics*, vol. 126. New York, NY, USA: Oxford Univ. Press, 1998.
[51] R. W. Erickson and D. Maksimovic, "Basic magnetics theory, " in, *Fundamentals of Power Electronics*. Boston, MA, USA: Kluwer, 2001.
[52] M. Chen, M. Araghchini, K. K. Afridi, J. H. Lang, C. R. Sullivan, and D. J. Perreault, "A systematic approach to modeling impedances and current distribution in planar magnetics," in *Proc. IEEE Workshop Control Modeling Power Electron.*, Jun. 2014, pp. 1–17.
[53] H. C. Roters, *Electromagnetic Devices*. New York, NY, USA: Wiley, 1970.
[54] A. Balakrishnan, W. T. Joines, and T. G. Wilson, "Air-gap reluctance and inductance calculations for magnetic circuits using a Schwarz-Christoffel transformation," *IEEE Trans. Power Electron.*, vol. 12, no. 4, pp. 654–663, Jul. 1997.
[55] A. F. Hoke and C. R. Sullivan, "An improved two-dimensional numerical modeling method for e-core transformers," in *Proc. IEEE Appl. Power Electron. Conf. Expo.*, 2002, vol. 1, pp. 151–157.
[56] V. Valchev, A. van den Bossche, and T. Filchev, "2-D FEM tuned analytical approximation for fringing permeances," in *Scientific Computing in Electrical Engineering*. New York, NY, USA: Springer, 2004, pp. 399–407.
[57] J. Muhlethaler, J. W. Kolar, and A. Ecklebe, "A novel approach for 3D air gap reluctance calculations," in *Proc. IEEE Int. Conf. Power Electron., ECCE Asia*, 2011, pp. 446–452.
[58] F. E. Terman, "Section II: Circuit elements," in *Radio Engineers' Handbook*, 1st ed. New York, NY, USA: McGraw-Hill, 1943.
[59] L. F. Casey, A. F. Goldberg, and M. F. Schlecht, "Issues regarding the capacitance of 1–10 MHz transformers," in *Proc. IEEE Appl. Power Electron. Conf. Expo.*, Feb. 1–5, 1988, pp. 352–359.
[60] W. M. Chew, P. D. Evans, and W. J. Heffernan, "High frequency inductor design concepts," in *Proc. IEEE Power Electron. Spec. Conf.*, Jun. 24–27, 1991, pp. 673–678.
[61] W. H. Hayt, and J. E. Kemmerly, "Inductance and capacitance: Duality," in *Engineering Circuit Analysis*, 4th ed. New York, NY, USA: McGraw-Hill, 1993.
[62] D. C. Hamill, "Lumped equivalent circuits of magnetic components: The gyrator-capacitor approach," *IEEE Trans. Power Electron.*, vol. 8, no. 2, pp. 97–103, Apr. 1993.
[63] M. A. Bahmani, T. Thiringer, and H. Ortega, "An accurate pseudoempirical model of winding loss calculation in HF foil and round conductors in switchmode magnetics," *IEEE Trans. Power Electron.*, vol. 29, no. 8, pp. 4231–4246, Aug. 2014.

Minjie Chen (S'10) received the B.S. degree in electrical engineering from Tsinghua University, Beijing, China, in 2009, and the S.M. and E.E. degrees from the Massachusetts Institute of Technology (MIT), Cambridge, MA, USA, in 2012 and 2014, respectively, where he is currently working toward the Ph.D. degree.

His research interest includes high-frequency, high-power density, and high-performance power electronics, focusing on distributed and sophisticated power conversion architecture that can enhance the figure-of-merits of power electronics systems.

Dr. Chen received the National Outstanding Student Scholarship from Tsinghua University, and the E.E Landsman Fellowship from MIT.

Mohammad Araghchini (S'08–M'14) received the B.S. degree in electrical engineering from University of Tehran, Tehran, Iran, and the S.M. and Ph.D. degrees in electrical engineering and computer science from Massachusetts Institute of Technology (MI), Cambridge, MA, USA, in 2008 and 2013, respectively, where he received the Electrical Engineer's degree.

He is currently a Postdoctoral Associate at the MIT. His current research interests include analysis, design, optimization, and fabrication of microscale magnetic components for high-frequency integrated power electronics.

Khurram K. Afridi (S'93–M'98) received the B.S. degree in electrical engineering from the California Institute of Technology, Pasadena, CA, USA, in 1989, and the S.M. and Ph.D. degrees in electrical engineering and computer science from the Massachusetts Institute of Technology (MIT), Cambridge, MA, USA, in 1992 and 1998, respectively.

During summers and between degrees, he was with JPL, Lutron, Philips, and Schlumberger. In 1997, he joined the founding team of Techlogix as the Chief Technology Officer and became the Chief Operating Officer in 2000. From 2004 to 2008, he also led the development of LUMS School of Science and Engineering as the Project Director, and was appointed an Associate Professor and the Werner-von-Siemens Chair for Power Electronics in 2008. From 2009 to 2014, he was a Visiting Associate Professor with the Department of Electrical Engineering and Computer Science, MIT. Since January 2014, he has been an Assistant Professor at the Department of Electrical, Computer, and Energy Engineering, University of Colorado, Boulder, CO, USA. His research interests include power electronics and energy systems incorporating power electronic controls.

Dr. Afridi received the Carnation Merit Award from Caltech and the BMW Scientific Award from BMW AG.

Jeffrey H. Lang (S'78–M'79–SM'95–F'98) received the S.B., S.M., and Ph.D. degrees from the Department of Electrical Engineering and Computer Science, Massachusetts Institute of Technology (MIT), Cambridge, MA, USA, in 1975, 1977, and 1980, respectively.

He was the Associate Director with the MIT Laboratory for Electromagnetic and Electronic Systems between 1991 and 2003. He joined the faculty of MIT in 1980, where he is currently the Vitesse Professor of electrical engineering. His research and teaching interests include the analysis, design, and control of electromagnetic and electromechanical systems with an emphasis on rotating machinery; micro/nanoscale (MEMS/NEMS) sensors, actuators and energy converters; flexible structures; and the dual use of electromechanical actuators as motion and force sensors. He has written more than 260 papers and holds 12 patents in the areas of electromechanics, MEMS, and power electronics and applied control. He served as an Associate Editor of *Sensors and Actuators* between 1991 and 1994. He has also served as the General Cochair and the Technical Cochair of the 1992 and 1993 IEEE MEMS Workshops, respectively, and the General Cochair of the 2013 PowerMEMS Conference. He is a Coauthor of *Foundations of Analog and Digital Electronic Circuits* (San Mateo, CA, USA: Morgan Kaufman, 2005), and the Editor of, and a contributor to, *Multi-Wafer Rotating MEMS Machines: Turbines Generators and Engines* (New York, NY, USA: Springer, 2009).

Prof. Lang is a former Hertz Foundation Fellow. He received the four best-paper prizes from IEEE societies, and has received two teaching awards from MIT.

Charles R. Sullivan (S'93–M'96–SM'12–F'14) received the B.S.(Hons.) degree in electrical engineering from Princeton University, Princeton, NJ, USA, in 1987, and the Ph.D. degree in electrical engineering from the University of California, Berkeley, CA, USA, in 1996.

Between the B.S. and Ph.D. degrees, he was with Lutron Electronics designing electronic ballasts. He is currently a Professor at the Thayer School of Engineering at Dartmouth, Hanover, NH, USA. His research interests include design optimization of magnetics for high-frequency power conversion, thin-film magnetic materials, and devices for power applications, energy efficiency, and renewable energy, and electromagnetic modeling of capacitors.

Dr. Sullivan received the National Science Foundation CAREER Award and two Power Electronics Society Prize Paper Awards.

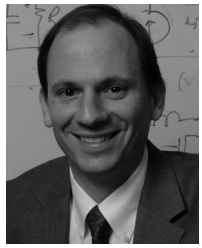

David J. Perreault (S'91–M'97–SM'06–F'13) received the B.S. degree from Boston University, Boston, MA, USA, and the S.M. and Ph.D. degrees from the Massachusetts Institute of Technology (MIT), Cambridge, MA.

In 1997, he joined the MIT Laboratory for Electromagnetic and Electronic Systems as a Postdoctoral Associate, and became a Research Scientist within the laboratory in 1999. In 2001, he joined the MIT Department of Electrical Engineering and Computer Science, where he is currently a Professor and an Associate Department Head. He also consults widely in industry, and is the Cofounder of Eta Devices, a startup company focusing on high-efficiency RF power amplifiers. His research interests include design, manufacturing, and control techniques for power electronic systems and components, and in their use in a wide range of applications.

Dr. Perreault received the Richard M. Bass Outstanding Young Power Electronics Engineer Award from the IEEE Power Electronics Society, an ONR Young Investigator Award, and the SAE Ralph R. Teetor Educational Award, and is the Coauthor of six IEEE prize papers.